AGU PUBLICATIONS

JGR

Journal of Geophysical Research: Atmospheres

RESEARCH ARTICLE
10.1002/2013JD020714

Key Points:
- Aerosol-radiation-cloud interactions and feedbacks is the main focus
- Integrated modeling approach (use of model RAMS/ICLAMS) is adopted
- Indirect effects affect precipitation more than direct and semi-direct

Correspondence to:
G. Kallos,
kallos@mg.uoa.gr

Citation:
Kushta, J., G. Kallos, M. Astitha, S. Solomos, C. Spyrou, C. Mitsakou, and J. Lelieveld (2014), Impact of natural aerosols on atmospheric radiation and consequent feedbacks with the meteorological and photochemical state of the atmosphere, *J. Geophys. Res. Atmos.*, *119*, 1463–1491, doi:10.1002/2013JD020714.

Received 8 AUG 2013
Accepted 20 DEC 2013
Accepted article online 23 DEC 2013
Published online 7 FEB 2014

Impact of natural aerosols on atmospheric radiation and consequent feedbacks with the meteorological and photochemical state of the atmosphere

J. Kushta[1,2], G. Kallos[1], M. Astitha[1,3], S. Solomos[1], C. Spyrou[1], C. Mitsakou[1,4], and J. Lelieveld[2,5]

[1]University of Athens, School of Physics, University of Athens Campus, Athens, Attiki, Greece, [2]Energy, Environment, and Water Research Centre, The Cyprus Institute, Nicosia, Cyprus, [3]University of Connecticut, Civil and Environmental Engineering, Storrs, Connecticut, USA, [4]King's College London, Environmental Research Group, London, UK, [5]Max Planck Institute for Chemistry, Hahn-Meitnerweg 1, Mainz, Germany

Abstract This paper addresses the aerosol effects on radiation and the feedback on meteorology and photochemical activity, applying the online model RAMS/ICLAMS. The model treats meteorology and chemical pollutants on an interactive way. Cloud condensation nuclei (CCN), giant cloud condensation nuclei, and ice nuclei are treated as predictive quantities. The calculation of the aerosol optical properties accounts for size-resolved mineral dust and size- and humidity-dependent optical properties of sea salt. The simulations with and without aerosol impacts reveal the complex direct and indirect mechanisms through which the alteration of radiation fluxes influences meteorology and photochemical processes. For the specific dust event, the reduction in the surface shortwave radiation over cloudless regions affected by dust averages at ~ $-75\,W\,m^{-2}$ at 12:00 UTC per unit dust loading ($1\,g\,m^{-2}$). The increase on downwelling longwave radiation over the same areas and time averages at ~ $40\,W\,m^{-2}$ per unit dust loading ($1\,g\,m^{-2}$). Surface upwelling longwave radiation over Mediterranean exhibits a complex daytime behavior. During midnight, the inclusion of dust leads to larger upwelling longwave radiation fluxes over the African continent. The net downward longwave radiation over cloudless areas exhibits an increase both during noon and midnight with the inclusion of dust. The results show that the vertical structure of the dust layer governs the magnitude of the feedback on radiation. The activation of natural particles as CCN causes small changes in radiation fluxes and temperature. Precipitation is influenced more by the indirect rather than the direct and semidirect effects.

1. Introduction

Atmospheric pollutants of natural and anthropogenic origin have significant impacts on climate, air quality, weather, and human health, often with uncertain underlying processes [*Haywood and Boucher*, 2000; *Jacobson*, 2001; *Lohmann and Feichter*, 2005; *IPCC*, 2007; *Lau and Kim*, 2007; *Andreae and Rosenfeld*, 2008; *Mitsakou et al.*, 2008]. Aerosols influence the climate directly through absorbing and scattering the incoming solar radiation, semidirectly through the changes in cloud distribution caused by their interaction with radiation and indirectly by acting as cloud condensation and ice nuclei, thus altering cloud properties and precipitation patterns and intensity [e.g., *Nenes et al.*, 2002; *Teller and Levin*, 2006; *Forster et al.*, 2007; *Rosenfeld et al.*, 2008; *Solomos et al.*, 2011; *Spyrou et al.*, 2013]. The atmospheric changes initially caused by the aerosols feed back onto the chemical and physical properties of gases and particles. The complexity of these feedbacks corroborates the importance of implementing integrated air quality and chemical weather modeling tools, together with measurement techniques, in order to accurately describe and understand the complex mechanisms involved [*Grell and Baklanov*, 2011]. Studies of the relevant links and feedbacks between the different processes can be performed with this fully online approach, the integral employment of the meteorological and chemical mechanisms (at the same spatial and temporal resolution, same parameterization, and a higher frequency of data exchange).

Several studies have evaluated the direct impact of aerosols on radiation altering the photolytic rates and ozone production in the atmosphere using zero or one-dimensional (0D or 1D), radiative transfer (RTM), or box models [*Dickerson et al.*, 1997; *Liao et al.*, 1999; *Castro et al.*, 2001]. *Jacobson* [1998] was one of the first to realize a three-dimensional modeling study of the impact of aerosols on the photolysis rates and atmospheric temperature concluding that, over the urban area of Los Angeles, aerosols can decrease surface

photolysis rates of ozone by 5–8%. Studies that have analyzed the aerosol effect on the photolysis rates with the use of offline chemical transport models (CTM) include those of *Li et al*. [2005], and *Real and Sartelet* [2011], among others. *Li et al*. [2005] found a 10–30% reduction in the photolysis rates and a corresponding ozone reduction of 5–20% from black carbon alone. *Real and Sartelet* [2011] found that the reduction of the solar radiation from various aerosol species can cause a reduction in NO and OH by 14% and ozone by 3% on a monthly average basis. Another CTM and observational study over East Asia-Western Pacific [*Tang et al*., 2003] recognized a larger effect of the aerosol mixtures (soil dust and anthropogenic) on the photochemistry of the region compared to that of clouds. On a global scale, *Martin et al*. [2003] and *Bian et al*. [2003] utilized CTMs and concluded that the impact of aerosols on photochemistry is relatively large in the Northern Hemisphere due to anthropogenic activity and mineral dust sources and may, on average, increase tropospheric O3. *Li et al*. [2011] used WRF/CHEM to study the organic aerosol effects on photochemistry over Mexico city for two three-day pollution episodes finding a more significant decrease in the photolysis rates due to aerosols during early morning and late afternoon hours (10–30%) than during noon hours (7–10%). As a consequence of the reduction in the photolysis rates, the O3 levels in the area decreased by 5–20%, respectively. These results agree with those obtained from *Castro et al*. [2001] with the use of observational data and the Tropospheric Ultraviolet and Visible Radiation Model (TUV) calculations in the same city but are larger than those of *Jacobson* [1998] for Los Angeles. The reason for the differences in these studies may be explained by the study of *Stockwell and Goliff* [2004], who suggested that the impact of photolysis rates on O3 concentrations may vary depending on the ratio of volatile organic compounds (VOCs) to NOx (NO + NO2), leading to different reductions for different areas.

Focusing on the Eastern Mediterranean region (EMR), *Benas et al*. [2013] conducted a modeling study of the photolysis rates of JO1D (O3 to O2 and O1D) for the 2000–2010 period, using an RTM with a resolution of 50 km × 50 km and climatological data from the Moderate Resolution Imaging Spectroradiometer (MODIS). According to their study, the decrease in the photolysis rates due to aerosols can exceed 10% during dust events and reach a median value of 2.3% over the whole period considered. *Gerasopoulos et al*. [2012], on the other hand, with a mainly observational study for the 2002–2006 period, concluded that for regional background aerosol pollution (aerosol optical depth (AOD) = 0.1) the reduction on the JO1D and JNO2 (NO2 to NO and O) is less than 6% while during dust events the reduction can reach 30–40% at high solar zenith angle. *Astitha and Kallos* [2008] in a previous study that utilized dust-corrected photolysis rates calculated by TUV gave a reduction of 14–15% in JO1D and JNO2 by a dust optical depth (DOD) of 0.55 and as much as 20% for a DOD of about 0.7–0.8.

Studies that investigated the aerosol radiative forcing with the use of coupled meteorological and chemical modeling systems include the work of *Fast et al*. [2006], *Stanelle et al*. [2010], *Vogel et al*. [2009], and *Bangert et al*. [2011]. *Fast et al*. [2006] found a reduction of ~ −20 to −30 W m^{-2} for a modeled AOD415nm of 0.2–0.3 with organic carbon and SO4-2 making up the largest fraction of their PM2.5 aerosol mass. They also performed a sensitivity test in order to see the impact of these aerosols on the photochemistry and showed an increase in the photolysis rates in the absence of aerosols (5%), 10–20 ppbV more ozone in the urban plume but lower ozone concentrations in other locations indicating a nonmonotonous response of the ozone levels to the changes in the photolysis rates. *Stanelle et al*. [2010] focused on dust episodes and their impact on the atmospheric processes over West Africa. They found a linear reduction in shortwave radiation that averaged at −140 W m^{-2} and a nonlinear longwave radiation response with an average decrease in the net longwave flux of 70 W m^{-2}, both at noon time and for an AOD450nm of 1. *Vogel et al*. [2009] and *Bangert et al*. [2011] studied the direct and indirect effect of soot and secondary aerosols on the state of the atmosphere, but they both excluded mineral dust as it was not the main contributor of the PM10 aerosol mass and affected only a small part of their domain. *Solomos et al*. [2011] focused on the impact of prognostically calculated natural aerosols (mineral dust and sea salt) on clouds and precipitation, corroborating the intricate links between aerosol properties and the spatiotemporal precipitation distribution. *Forkel et al*. [2012] extended the investigation to study the effect of aerosols on radiation and meteorological parameters as well as regional air quality. They found that the enhanced photochemical activity over areas with increased solar radiation can result either in an increase or a decrease in ozone levels. The sign of the response is determined by the pollution level of the area. Low pollution levels lead to ozone destruction when photochemical activity is enhanced, while the situation is opposite for areas with sufficiently high levels of NOx and VOC.

Table 1. RAMS/ICLAMS Configuration Options

Basic Equations	Nonhydrostatic Time Split Compressible
Dimensionality	Three dimensional
Vertical coordinate	Terrain following height coordinate
Horizontal coordinate	Lambert conformal transformation
Grid structure	Arakawa-C grid stagger
Time differencing	Hybrid combination of leapfrog and forward in time
Turbulence closure	Mellor-Yamada level 2.5 scheme-ensemble averaged TKE [*Mellor and Yamada*, 1982]
Cloud microphysics	Warm rain processes Five ice condensate species Two-moment bulk scheme [*Walko et al*., 1995; *Meyers et al*., 1997]. Cloud droplet activation scheme [*Nenes and Seinfeld*, 2003; *Fountoukis and Nenes*, 2005] (ACTIVATED for grid scale clouds)
Convective parameterization	Kain-Fritsch cumulus parameterization
Radiation	Rapid Radiative Transfer Model (RRTM) [*Mlawer et al*., 1997; *Iacono et al*., 2008] with mineral dust and sea-salt radiative effects on radiation as a function of size and water content (ACTIVATED)
Aerosol parameterization	Mineral Dust online emission scheme (eight-size bins) Sea-salt spray online emission scheme (accumulation and coarse mode) Anthropogenic aerosols (primary emissions and chemical formation) (nucleation, accumulation, and coarse mode; lognormal distributions) Dry deposition of natural and anthropogenic aerosols Wet deposition of natural and anthropogenic aerosols
Emissions	Anthropogenic emissions for 2005 (JRC 0.1° × 0.1° global emissions of CO2, NH3, CH4, SO2, NOx, CO, N2O, VOCs, OC, and BC) Biogenic emissions [*Guenther et al*., 1995]
Chemistry parameterization	Online calculation of photodissociation rates Online gas, aqueous, and aerosol phase chemistry (SAPRC99, ISORROPIA) Dry and wet deposition of gaseous pollutants
Lower boundary	Soil-vegetation-snow parameterization (LEAF-3) [*Walko et al*., 2000]
Boundary conditions	*Klemp and Wilhelmson* [1978] radiative condition
Initialization	LAPS 3-D data assimilation preprocessing system

The main topic of this work is to assess the impact of different types of aerosols on the atmospheric radiation budget and subsequently on photochemical processes. The objectives addressed in this paper are:

1. Assess the direct, semidirect, and indirect effects of desert dust particles.
2. Study feedback mechanisms by the above processes through their influence on the atmospheric conditions and photochemistry.
3. Investigate the effects of sea-salt particles on radiation and precipitation processes.
4. Demonstrate the relative contributions of these aerosol types and their combined effects on atmospheric conditions.

The novelty of this approach, compared to previously published work, is related to the fully coupled integrated modeling system with state-of-the-art atmospheric and chemical modules that allow the quantification of the direct, semidirect, and indirect aerosol effects (by switching on and off the feedback mechanisms) and the investigation of their importance for the area considered. This work focuses on the EMR that is a crossroad of anthropogenic and natural pollutants and an area of intense photochemical activity due to strong insolation in the summer period [*Lelieveld et al*., 2002]. In addition, measurements of photolytic frequencies are available from *Gerasopoulos et al*. [2006, 2012]. The new model capabilities that are modified and utilized in this study are shown in Table 1. The model's activated processes that are important to the scope of this work are described in section 2 and the model configuration in section 2.2. The results from the simulations and the comparison with the observations are presented in section 3 and a discussion and summary are given in section 4.

2. RAMS/ICLAMS Description

The Regional Atmospheric Modeling System (RAMSv6) [*Cotton et al*., 2003] is the core model used for the development of the Integrated Community Limited Area Modeling System (RAMS/ICLAMS) [*Solomos et al*., 2011]. RAMS/ICLAMS is a coupled meteorology-chemistry modeling system developed as a forecasting and

Table 2. Mineral Dust and Sea-Salt Particle Properties That Are Used for Their Cloud Condensation Nuclei (CCN) and Ice Nuclei (IN) Activation

	Mineral Dust	Sea Salt
CCN activation	Yes	Yes
IN activation	Yes	No
Percentage that can be activated as CCN (maximum permitted)	10%	100%
Percentage that can be activated as IN (maximum permitted)	100%	0%

research tool for process studies, air pollution, and regional climate applications. The fully coupled approach is applied to all processes that influence pollutant transport and transformation, chemistry-microphysical interactions, and the direct and indirect feedbacks of gas and aerosol pollutants on the heating rates and photolysis rates, as well as cloud properties and precipitation, in one single modeling core. Previous work with the model [*Solomos et al*., 2011] focused on the impact of mineral dust and sea salt on several meteorological processes, such as cloud development and precipitation patterns, without the utilization of the online chemical components. The air quality submodel considers emissions, photo-dissociation reactions, gas and aqueous phase chemical transformations, aerosol processes, aerosol-radiation-cloud interactions, and removal mechanisms. A brief summary of the modules included is presented below.

The parameterization of dust emissions is based on the saltation and bombardment approach as described in *Marticorena et al*. [1997] utilizing eight bins for the dust transport size distribution with effective radius of 0.15, 0.25, 0.45, 0.78, 1.3, 2.2, 3.8, and 7.1 μm [*Perez et al*., 2006; *Spyrou et al*., 2010]. The performance of this parameterization scheme as implemented in RAMS/ICLAMS has been evaluated for Saharan dust in the work of *Solomos et al*. [2011] and *Solomos et al*. [2012]. Sea-salt emissions, using two size bins (accumulation and coarse), follow the open sea white-cap formation [*Monahan et al*., 1986; *Gong*, 2003; *Zhang et al*., 2005] and the coastline sea-salt flux parameterization described in *Leeuw et al*. [2000]. Dust and sea-salt particles are not chemically speciated in the model. The biogenic emissions are calculated online following the method described in *Guenther et al*. [1995]. The photochemical scheme uses the basic formulations proposed by *Madronich* [1987]. The gas phase chemistry module is based on the chemistry mechanism of the State-wide Air Pollution Research Center, Version 1999-SAPRC99 [*Carter*, 2000; *Carter et al*., 2003]. The aqueous chemistry submodule calculates the changes in pollutant concentrations due to interaction of gases with droplets [*Walcek and Taylor*, 1986]. Cloud droplet nucleation parameterization follows *Fountoukis and Nenes* [2005]. This scheme is an extension of the bin sectional methodology of *Nenes and Seinfeld* [2003] and accounts for bulk lognormal aerosol size distributions.

The formation of ice nuclei (IN) is also calculated online with the scheme of *Barahona and Nenes* [2009]. The main aerosol characteristics regarding CCN and IN activation of the dust and sea-salt particles in this application are summarized in Table 2. Dust particles can act as both CCN (up to 10% of their number concentration) and IN (up to 100%) while sea-salt particles can only be activated as CCN. The soluble mass fraction of the particles is assumed to be 0.33 for mineral dust and 1 for sea salt. The model is initialized with a horizontally uniform concentration of 4×108 CCN per kg of air and 1×105 IN per kg of air, based on considerations from several previous studies [e.g., *DeMott et al*., 2003; *Levin et al*., 2005; *Klein et al*., 2010]. For the IN parameters freezing threshold, wettability parameter, and maximum freezing efficiency, the used values are 0.2, 0.96, and 0.05, respectively. More information on the IN properties can be found in the cited publication. Anthropogenic aerosols are not utilized as CCN or IN and are not included in the cloud interaction processes in this configuration.

The aerosol composition is based on the Model-3 Community Multiscale Air Quality (CMAQ) method as described in *Binkowski and Roselle* [2003] and the aerosol treatment is derived from the Regional Particulate Model (RPM) [*Binkowski and Shankar*, 1995]. The aerosol size distribution follows a modal approach using three lognormal distribution modes that include the aitken ($D = 0.01$–0.1 μm), the accumulation ($D = 0.1$–2.5 μm), and the coarse mode ($D > 10$ μm). The inorganic thermodynamic processes are treated by the ISORROPIA equilibrium model [*Nenes et al*., 1998] and the formation of the secondary organic aerosol (SOA) is based on the work of *Schell et al*. [2001]. Finally, the dry deposition module is based on the resistance model of *Wesely* [1989]. RAMS/ICLAMS components that are important for the study of the aerosol effects and feedbacks on radiation are described in the following paragraphs.

2.1. Radiation Scheme and Aerosol Optical Properties

The Rapid Radiative Transfer Model-GCM (RRTMG) is used for both shortwave and longwave radiation transfer [*Mlawer et al*., 1997; *Iacono et al*., 2008; *Spyrou et al*., 2013]. RRTMG uses 14 spectral bands to represent the shortwave spectrum and 16 spectral intervals for the longwave spectrum. Of the shortwave bands, four are important for all photolytic processes except for O3P that is active in five bands. Aerosol radiative effects are treated in RRTMG through the specification of their optical properties within each spectral interval. The optical properties of mineral dust and sea salt are calculated online depending on size distributions and relative humidity.

The aerosol optical thickness at each wavelength $\tau(\lambda,z)$ is calculated by the following formula:

$$\tau(\lambda,z) = \sum_{i=1}^{N} \frac{3}{4\rho_i r_i} AL_i(z) Q_{ext,i}(\lambda,z) \quad (1)$$

where N is the number of particle size bins, ρ is the particle density (kg m^{-3}), r is the particle radius (m), $AL(z)$ is the aerosol load of each layer (kg m^{-2}), and $Q_{ext,i}(\lambda,z)$ (unitless) is the extinction efficiency calculated from the Mie theory [*Tegen and Lacis*, 1996; *Perez et al*., 2006; *Spyrou et al*., 2013] using optical parameters from the software package OPAC (Optical Properties of Aerosols and Clouds) [*Hess et al*., 1998]. In the case of sea-salt particles the extinction efficiencies are produced taking into account the growth of the aerosol radius and the change of the optical properties under different humidity values. The cloud hydrometeors are divided into seven main groups (cloud, rain, ice, graupel, snow, pristine, and aggregates) that are all utilized in the calculation of the radiation budget. The optical properties of clouds can be either computed from the microphysical submodel [*Meyers et al*., 1997] or calculated from a separate routine in the RRTMG radiation submodel [*Iacono et al*., 2008 and references therein]. In the present test case we utilized the calculation from the RRTMG radiation submodel.

2.2. Calculation of the Photolysis Rates

The photochemical scheme uses the basic formulations proposed by *Madronich* [1987]. There are 25 reactions that represent atmospheric photochemistry as described in the "Implementation of the SAPRC-99 Chemical Mechanism into the Models-3 framework," report to the United States Environmental Protection Agency, by William P. L. Carter, 2000. (http://www.cert.ucr.edu/~carter/pubs/s99mod3.pdf). The set of equations for the chemical reactions kinetics and species conservation that describe the variation in time of the species concentrations and their rate of formation and/or depletion are solved with the use of the chemistry solver Euler Backward Iterative algorithm (EBI) [*Hertel et al*., 1993].

Photolysis rates for the photolytic reactions are computed as the product of the absorption cross section, quantum yield, and actinic flux, integrated over all relevant wavelengths:

$$\left(\frac{d[X]}{dt}\right)_{\text{reac } i} = -[X]\cdot\int \sigma_X(\lambda)\ \ \phi_i(\lambda,T)\ \ E(\lambda)\ \ d\lambda \quad (2)$$

where $\frac{d[X]}{dt}$ is the rate of change of concentration X of species x during the photolytic reaction i, $\sigma_X(\lambda)$ is the absorption cross section of species x, $\phi_i(\lambda,T)$ the quantum yield of reaction i as a function of wavelength and temperature, and $E(\lambda)$ the spectral actinic flux over the wavelength range $d\lambda$. The absorption cross sections and quantum yields are summarized in the documentation of the SAPRC-99 chemical mechanism for VOC reactivity assessment [*Carter*, 2000]. The total actinic flux and consequently the photolysis rates are simulated at each grid point of the model domain and can be updated at the spatial and temporal resolution of the meteorological model. However for numerical efficiency, the photolysis module is activated at a frequency equal to that of the radiation update (600 s).

One advantage of the online approach is that the dependence of the absorption cross sections on temperature and pressure can be continuously monitored and reflected in the values of the photolysis rates. Moreover, the approach adopted here allows the straightforward determination of the actinic flux considering modifications due to absorption by aerosols, ozone, water vapor, CO2, Rayleigh scattering, and detailed absorption and scattering by clouds, rather than implementing classical techniques where the clear-sky photodissociation rates are corrected based on cloud fraction.

3. Model Configuration and Structure of the Sensitivity Simulations

The topography and vegetation data are derived from the US Geological Survey (USGS) 30″ × 30″ data set and the soil texture from Zobler and FAO/UNESCO at 2′ × 2′ resolution. A high-resolution reanalysis data set is used for the initial and lateral boundary conditions of the meteorological parameters at a resolution of 0.15° × 0.15°. This data set has been produced by downscaling 0.5° × 0.5° analysis data from the European Center for Medium-Range Weather Forecasts (ECMWF) that includes surface (including buoy and ship) and upper air observations (www.ecmwf.int). The frequency of the produced reanalysis fields is three hours. The 3-D Local Analysis and Prediction System-LAPS [*Albers et al*., 1996] is used for the preparation of the reanalysis data set (laps.noaa.gov). The National Center for Environmental Prediction (NCEP) 0.5° × 0.5° sea surface temperature analysis is used for water body initial conditions. Initial and boundary conditions of gaseous and anthropogenic aerosol species are taken from predefined vertical profiles. The concentrations in these profiles are given as a function of height on terrain following sigma coordinates. The vertical profiles for O3 are based on the work of *Fischer et al*. [2006] who have produced vertical, seasonal, and latitudinal distributions over Europe based on measurement campaigns within SPURT (SPURenstofftransport in der Tropopausenregion: Trace gas transport in the tropopause region) project [*Engel et al*., 2006]. The domain used in this study covers an area of 6000 km × 3600 km over the Greater Mediterranean Region (GMR) with a spatial resolution of 12 km. Vertically, the domain stretches up to 24.3 km with 34 layers, with the first layer located at 47 m above ground.

The emissions incorporated in the model are derived from a recently updated high-resolution global emission inventory (1990–2005) developed in the framework of the Climate Change and Impact Research: the Mediterranean project (CIRCE EU FP6 Project No. 036961), by the EDGAR group (Emission Database for the Global Atmospheric Research) of the EC-Joint Research Center, Ispra, Italy (JRC), Climate Change Unit. The emission inventory follows the methodology of the EDGAR tool [*Olivier et al*., 1999; *van Aardenne et al*., 2001]. EDGAR contains global anthropogenic emissions inventories of various air pollutants and greenhouse gases and is used to calculate anthropogenic emissions of air pollutants (gases and particles) and greenhouse gases (GHG) by sector and country, with a temporal resolution of a month and spatial resolution of 0.1° × 0.1° latitude-longitude. The anthropogenic emissions include the greenhouse gases CO2, CH4, N2O, ozone precursor gases (CO, NOx, NMVOC), SO2, NH3, and black carbon (BC) and organic carbon (OC). Emissions are calculated for the reference year 2005 and include 245 countries globally.

Model simulations are divided into three categories:

1. Simulation without aerosol effects on radiation and without aerosol CCN activation (Baseline case).
2. Simulation with aerosol direct effects on radiation (radiation forcing — RF). The intent of this run is to assess changes in the meteorological and photochemical fields derived from the changes in the radiation budget. Semidirect changes on the cloud distribution and the meteorological and photochemical parameters are also discussed.
3. Simulation with aerosol direct, semidirect, and indirect effect (radiation and cloud forcing — RFCF). This simulation has the characteristics of the RF case and additionally includes the explicit computation of cloud droplet activation (CCN and IN from mineral dust) that is added to the background field of nuclei used in the RF and baseline case.

The feedback of different aerosol types is modeled separately by utilizing the modular structure of the code. "SS" abbreviation refers to the simulations where sea salt has been included in the feedback scheme and "MDSS" refers to the simulations where both mineral dust and sea-salt particles are used in the radiative and cloud module.

In order to investigate the impact of natural particles on radiation, meteorological, and photochemical production, a case study during a period of intense dust mobilization and transport to EMR is selected. Between 15 and 19 April 2004 a dust outbreak from N. Africa transported significant loads of dust particles that reached Southern Greece on 17 April 17. The model is run for a spin-up period of five days (10 to 14 April 2004) in order to establish a more realistic background pattern of natural aerosols over the area. Desert dust and sea-salt particles initial conditions are zero and the correct spin-up time is chosen accordingly. While a five-day simulation (15–19 April) is enough to capture low level and short

Table 3. Total Precipitation (Total PCP) Integrated Over All Domain Cells and Maximum Precipitation (in mm) Over Central Mediterranean per day (24 h PCP) and for the Whole Simulation Period (120 h PCP), for Each of the Simulation Cases[a]

Simulation	Time Period	Total PCP (m)	Maximum PCP (mm)
Baseline (no aerosol)	15 April	36.56	65.15
	16 April	39.93	60.73
	17 April	23.15	39.48
	18 April	28.60	49.66
	19 April	26.28	53.56
	15–19 April	154.52	110.9
RF (dust only)	15 April	33.84	72.75
	16 April	40.92	66.46
	17 April	20.71	31.30
	18 April	28.48	42.75
	19 April	31.92	64.12
	15–19 April	155.87	109.9
RF_SS (salt only)	15 April	36.46	63.94
	16 April	40.07	63.60
	17 April	23.24	38.25
	18 April	28.54	53.28
	19 April	26.69	53.68
	15–19 April	154.99	109.6
RF_MDSS (salt and dust)	15 April	33.66	72.07
	16 April	40.94	71.61
	17 April	20.57	31.49
	18 April	28.22	42.43
	19 April	31.84	64.85
	15–19 April	155.23	111.3
RFCF (dust only)	15 April	34.61	59.02
	16 April	41.24	63.18
	17 April	21.12	34.52
	18 April	28.81	45.92
	19 April	33.45	66.52
	15–19 April	159.22	106.1
RFCF_MDSS (salt and dust)	15 April	34.85	58.72
	16 April	40.70	57.55
	17 April	21.05	32.45
	18 April	28.87	45.08
	19 April	33.37	66.51
	15–19 April	158.84	105.5

[a]The domain over which the statistics are derived is shown in Figure 4.2b with the red dashed box.

distance dust mobilization and transport from North Africa to Crete, the spin-up simulation reveals a long range transport path of mineral dust from Western Africa. The result is the establishment of a dust layer over Finokalia at about 9 km (maximum concentrations ~50–70 $\mu g\ m^{-3}$) during our test period. Two additional sensitivity tests during the same test period are performed in order to assess the relative contribution of sea-salt particles (separately from and synergistically with mineral dust) on the atmospheric processes (Table 3).

Observational resources used in this study include: measurements of the photolysis rates of O1D and NO2, meteorological parameters (wind, temperature), and ozone concentrations available at Finokalia station, Greece (35° 19′ N, 25° 40′ E, altitude 250 m above sea level) (Prof. Nikos Mihalopoulos, personal communication 2013). The photolysis rates are described in detail in *Gerasopoulos et al.* [2006, 2012]. Ozone measurements were also available for Akrotiri station, Greece (Prof. Mihalis Lazaridis, personal communication 2012), for Montelibretti station (Italy) from the European Monitoring and Evaluation Programme (EMEP) network (http://www.emep.int). PM10 measurements at Heraklion station in Crete also obtained by personal communication (Dr. Giorgos Kouvarakis, University of Crete). Precipitation data were available from the Tropical Rainfall Measuring Mission TRMM product 3B42 V7 (http://disc2.nascom.nasa.gov/daac-bin/Giovanni/tovas), meteorological data available from NCEP reanalysis data set (NCEP FNL Operational Global Tropospheric Analyses), and cloud cover data from EUMETSAT's Satellite Application Facility on Climate Monitoring (http://dx.doi.org/10.5676/EUM_SAF_CM/CLARA_AVHRR/V001).

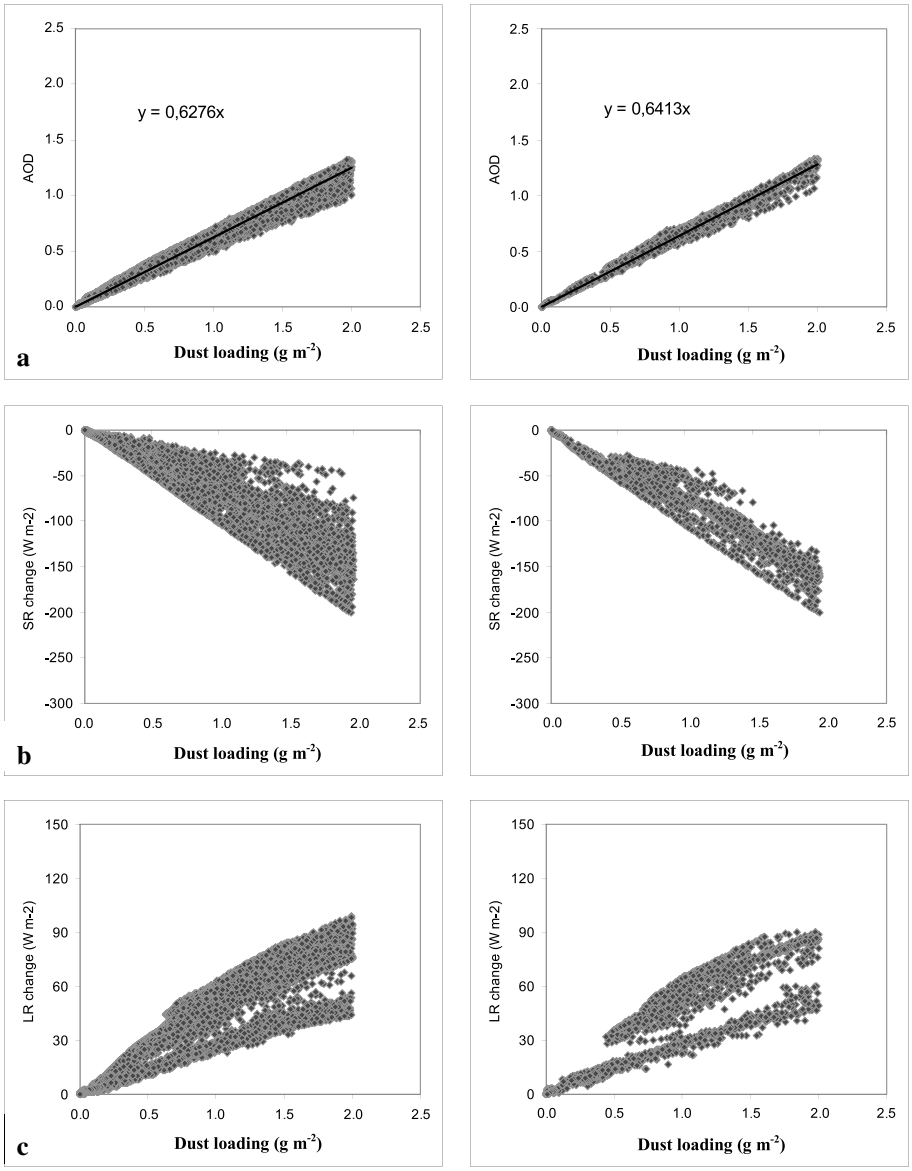

Figure 1. (a) Aerosol optical depth (AOD) as a function of total column dust load (g m^{-2}), difference in (b) the shortwave radiation (SR) in W m^{-2} expressed as SRRF − SRBASELINE and (c) in the downwelling longwave radiation (LR) in W m^{-2} expressed as LRRF − LRBASELINE on 17 April at 12:00 UTC (left plots) and 18 April 12:00 UTC (right plots) at the surface.

4. Results and Discussion

4.1. Dust Effects on Radiation

The microphysical and optical properties of dust particles determine their specific extinction cross section (σ), which is a measure of the relation between dust loading and its optical depth:

$$\sigma(\lambda) = \frac{\tau(\lambda)}{DL} \tag{3}$$

where $\tau(\lambda)$ is the AOD calculated in {1} and DL is the dust mass loading in g m^{-2}. As exhibited in Figure 1 (top plots), for dust loadings below 2 g m^{-2}, σ at the wavelength interval 441–625 nm is ~0.63–0.64. The 2 g m^{-2} threshold has been chosen to include areas that represent medium to large distances from dust sources for compliance with previous studies. These results are in good agreement with those obtained from *Gerasopoulos et al*. [2009] who found a specific extinction cross section of 0.64.

The direct feedback of dust on the radiation balance (RF) of the downwelling shortwave radiation at the surface (SR) is negative while the downwelling longwave radiation (LR) increases with the inclusion of dust. Figure 1 expresses the reduction in SR (middle plots) and LR (bottom plots) noted over all cloud-free grid cells (land and ocean surface cells that are cloud free in both baseline and RF runs) as a function of dust loading during noon. The radiative effect of mineral dust on LR is nonlinear. The attenuation of the SR with dust loading can be characterized as linear and expressed as $y = -71x$ for 17 April and $y = -79x$ for 18 April (where y is the absolute difference in SR and x the dust loading). The instantaneous decrease in SR at the surface for a dust loading of 1.5 g m^{-2} is 50–150 W m^{-2} on 17 April 12:00 UTC and 100–150 W m^{-2} on 18 April 12:00 UTC (~ −5 to v15%). For the same loading, LR at the surface increases by 30–80 W m^{-2} (~ +6 to +18%) constituting a net negative effect for dust of ~ −20 to −70 W m^{-2} per 1.5 g m^{-2} dust load. Using the dust forcing efficiency definition (ΔP/AOD where P is the respective radiation flux component) as described in *Helmert et al.* [2007], a value of −115 W m^{-2} per unit AOD is obtained for SR averaged over all cloudless domain cells. This result agrees with several similar studies. *Stanelle et al.* [2010] found an average forcing efficiency of −140 W m^{-2} for surface SR and an increase in surface LR of 70 W m^{-2} during noon for West Africa (per unit AOD calculated at 450 nm). *Helmert et al.* [2007] gave different values for southern and northern Sahara, respectively, −196 W m^{-2} to −220 W m^{-2} and −81 W m^{-2} to −85 W m^{-2} (per unit AOD calculated at 500 nm). Given the fact that different studies use AOD calculated at different wavelengths, a similar efficiency parameter can be obtained as ΔP/DL (where P is the respective radiation flux component and DL the total column dust load). Using this dust load forcing efficiency, the reduction in SR averaged over all cloudless domain cells reaches 75 W m^{-2} (per unit dust loading in g m^{-2}). The respective parameter for LR gives an average noon increase of 40 W m^{-2} over cloudless areas.

Terrestrial radiation (TR) (upwelling longwave radiation) is, in general, lower in the RF case than in the baseline case during daytime (Figure 2a). The instantaneous outgoing longwave radiation flux (upward) measured by the Aqua-AIRS 1° × 1° Level-3 product (http://disc.sci.gsfc.nasa.gov/giovanni) is in the range of 400–500 W m^{-2} in the dust source areas of N. Africa (not shown). These values are found to be more in line with the RF simulation. Dust constitutes a negative effect on TR, which is larger near the dust sources (−20 to −60 W m^{-2}), as depicted in Figure 2a. However, there are several areas, over the African continent as well as over the Balkans (indicated with the black circles in Figure 2a), where noon TR increases with the inclusion of dust. TR is a function of the temperature of the body that emits it and this complex behavior reflects the changes in surface temperature. As shown in Figure 2b, the 2 m air temperature (T2m) over these areas is also higher in the RF simulation. However, there are other areas with increased T2m that are not accompanied by a higher TR. When taking into account only the cloudless grid cells, the main feedback is positive (dust leads to larger TR). This result indicates that when there are no clouds, and therefore no changes in TR due to changes in the cloud distribution, the inclusion of dust (direct effect) warms the surface and leads to higher TR. The negative effect of dust on noon TR as shown in Figure 2a, even over areas where an increase in T2m is noticed, is mainly the result of the semidirect effect (the changes in the cloud distribution). The situation is opposite during the night when the TR of the RF case is larger than in the baseline case almost over all domain. The reversal happens after late afternoon (16–18 UTC) leading to nighttime TR increases of ~ +30 to +75 W m^{-2}. Combining the effect of dust on the LR with the effect of dust on the TR, an overall cloudless grid cells increase of ~ 65 W m^{-2} is noticed for net downwelling longwave radiation at noon and a smaller increase of 47 W m^{-2} is noticed during midnight. The daytime increase is therefore ~ 28% higher than nighttime increase. *Jacobson* [1997] gives a 31% higher daytime than nighttime increase in net downwelling longwave radiation.

Noon time surface heating rate reaches 3.6°K d^{-1} over Finokalia in the presence of dust that is two times higher than the respective value without dust (1.7°K d^{-1}). For comparison, *McFarlane et al.* [2009] reported a heating rate of 3–4°K d^{-1} over Niamey during a dust episode. Near surface heating rates were two times higher when dust particles were taken into account in the radiation budget. *Mohalfi et al.* [1998] gave a nonlinear increase in the heating rates over Saudi desert as a function of AOD with values 3, 4.5, and 6.5°K d^{-1} for AOD 0.5, 1.5, and 3.0, respectively. *Quijano et al.* [2000] also concluded that mineral aerosols produce a significant net heating where they are located and gave a value of ~ 2–3°K d^{-1} for cloudless conditions, DOD of 0.5, and cosine of zenith angle of 0.8. These values were 2–3 times higher than the HR without dust feedback. Over Africa the heating rates can reach locally 8–12°K d^{-1} during midday. *Mallet et al.* [2009] showed that during dust episodes over West Africa the heating rate at the surface can exceed 10°K d^{-1}.

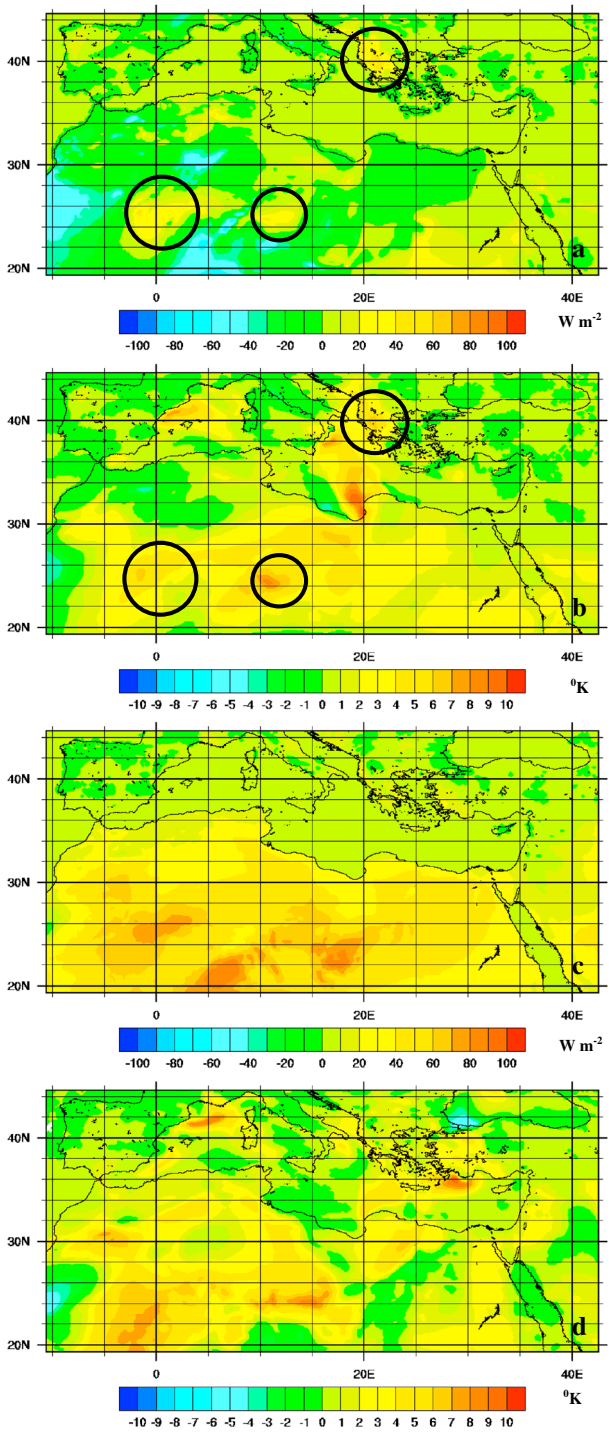

Figure 2. Difference in the upwelling longwave radiation (terrestrial radiation TR) in W m^{-2} expressed as TRRF − TRBASELINE on (a) 17 April at 12:00 UTC and (c) 18 April at 00:00 UTC at the surface and difference in 2 m air temperature (T2m) in °K expressed as TRF − TBASELINE on (b) 17 April at 12:00 UTC and (d) 18 April at 00:00 UTC.

4.2. Dust Feedback on Meteorological Parameters

Temperature, wind speed, accumulated rainfall, relative humidity, and total condensates are some of the affected atmospheric fields that will be discussed in this section. Total condensates refer to the sum of the mixing ratios of all condensates simulated by the microphysical scheme. By activating the interactive aerosol

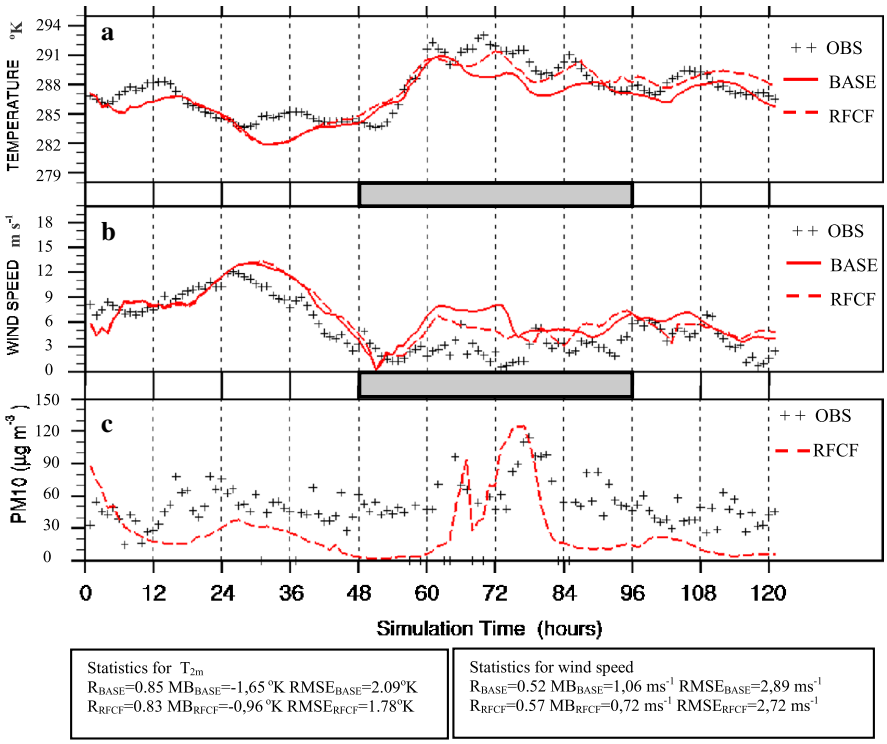

Figure 3. (a) Air temperature (T2m in °K), (b) wind speed (WS in m s^{-1}) as a function of the forecast hour (120 h from 15 to 19 April 2004) compared with measurements from the Finokalia station, Crete (35° 19′ N, 25° 40′ E, altitude 250 m above sea level), and (c) PM10 concentrations measured over Heraclion station, Crete (35° 20′ 12″ N, 25° 10′ 24″ E, altitude 39 m above sea level) and modeled sum of dust and sea-salt particles at the surface for the same time period. The crosses are the measured values, the red continuous line corresponds to the model results from the baseline case, and the red dashed line corresponds to the model results from the RFCF case. The gray box indicates the timeframe of the dust event. Time 0 of *x* axis corresponds to 15 April 2004, 00:00 UTC. Main statistical parameters are given below the plots for (left) T2m and (right) wind speed.

module it results in a difference of ~ 2.5°K in the T2m over Finokalia station, as illustrated in Figure 3a. The T2m simulated with the RFCF shows slightly better agreement with the observations than the baseline results, as indicated by the main statistical parameters and the time series. The correlation coefficient does not change (0.85 in the baseline case and 0.83 in the RFCF case) but the root mean square error (RMSE from 2.09°K in the baseline case decreases to 1.78°K in the RFCF) and the mean bias (MB decreases from −1.65°K in the baseline case to −0.96°K in the RFCF) improve with the inclusion of the dust feedback. The impact is also evident on the wind speed that decreases by 1–3 m s^{-1} during the same period (Figure 3b). The correlation coefficient from the comparison of modeled and observed wind speed improves from 0.52 in the baseline simulation to 0.57 in the RFCF simulation and the RMSE and MB decrease from 2.89 m s^{-1} to 2.72 m s^{-1} and from 1.06 m s^{-1} to 0.72 m s^{-1}, respectively. Therefore, the inclusion of the mineral dust feedback effects slightly improves the model performance for the aforementioned meteorological parameters during the days of the event (17–18 April 2004, 48–96 simulation hours).

In addition, aerosol measurements (PM10) from a neighbor meteorological station located in Heraclion, Crete, (35° 20′ 12″ N, 25 10′ 24″ E, altitude 39 m), are compared with the modeled dust and sea-salt concentrations of the RFCF simulation (Figure 3c). The model performed satisfactory during the days of the dust episode capturing the concentrations and the time of the event. During the previous days there is an evident underestimation of the observed PM10 concentrations that possibly refer to contribution from other local and regional sources of aerosols that are not included in this comparison. For 15 and 16 April 2004, this underestimation averages at ~ 35 μg m^{-3} under north-northwest winds (that dominate during that time period) and indicate transport of pollution from Central and East Europe as well as local pollution. It must be noted that Heraclion station is characterized as urban and is located close to Heraclion city, the largest city of the island of Crete.

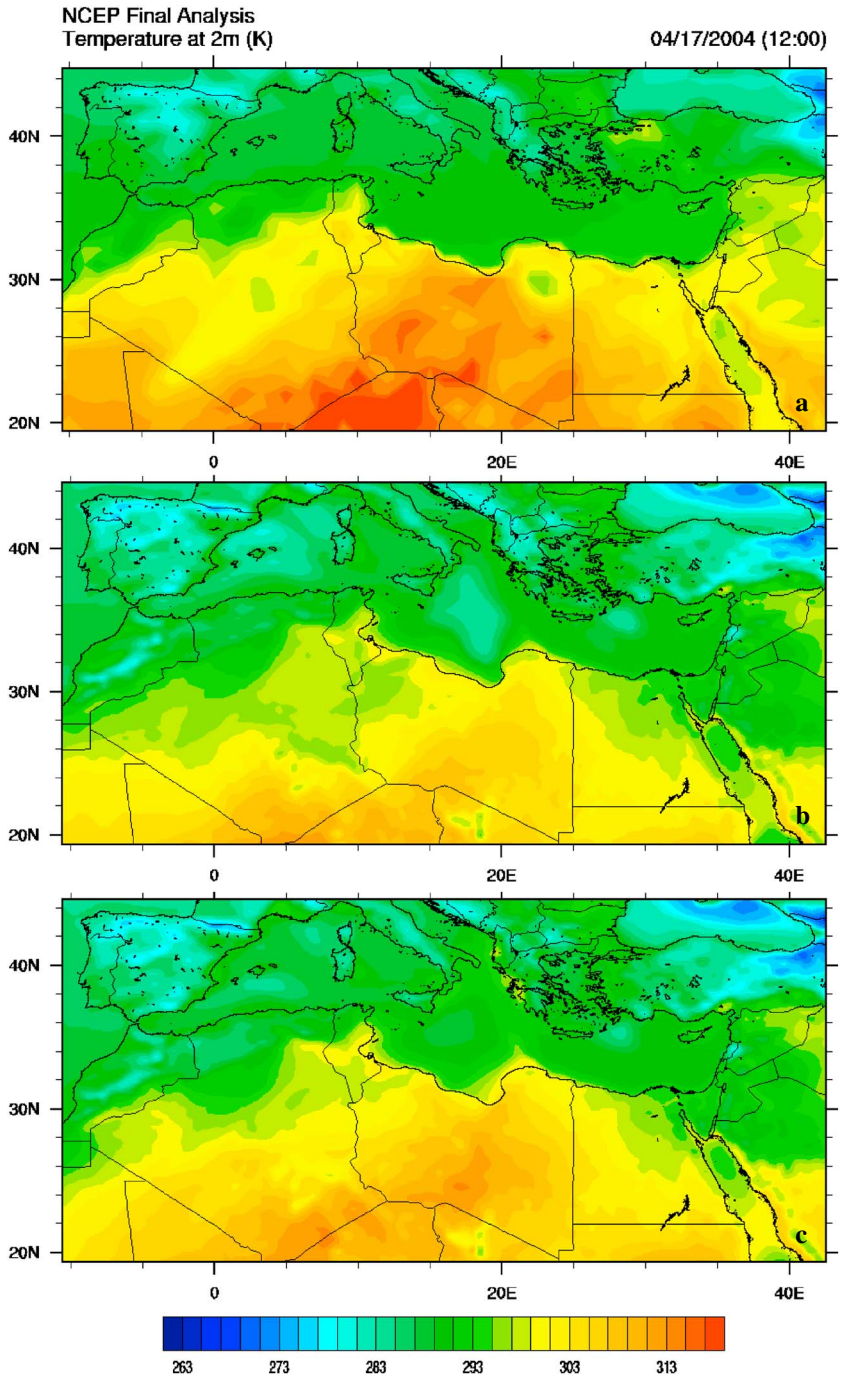

Figure 4.1. Air temperature T2m in °K (right plots) from (a) NCEP reanalysis, (b) baseline, and (c) RF model results on 17 April 2004, at 12:00 UTC.

Domain wide, the spatial patterns of the temperature field of the RF case are improved, following the NCEP Final Analysis T2m temperature patterns with a better agreement (Figure 4.1). In general, the T2m in the RF case over Africa is higher than in the baseline case. In particular, a warmer air mass over Libya and Algeria is noticed in RFCF, whereas the baseline simulation produces a 3–4°K cooler air temperature. Comparison of the accumulated precipitation from the five-day simulation with the TRMM satellite observations also reveals a slight improvement in the case where the feedback is included. The BASE run patterns underestimate accumulated rainfall over West Mediterranean. The RF simulation does not contribute much to the

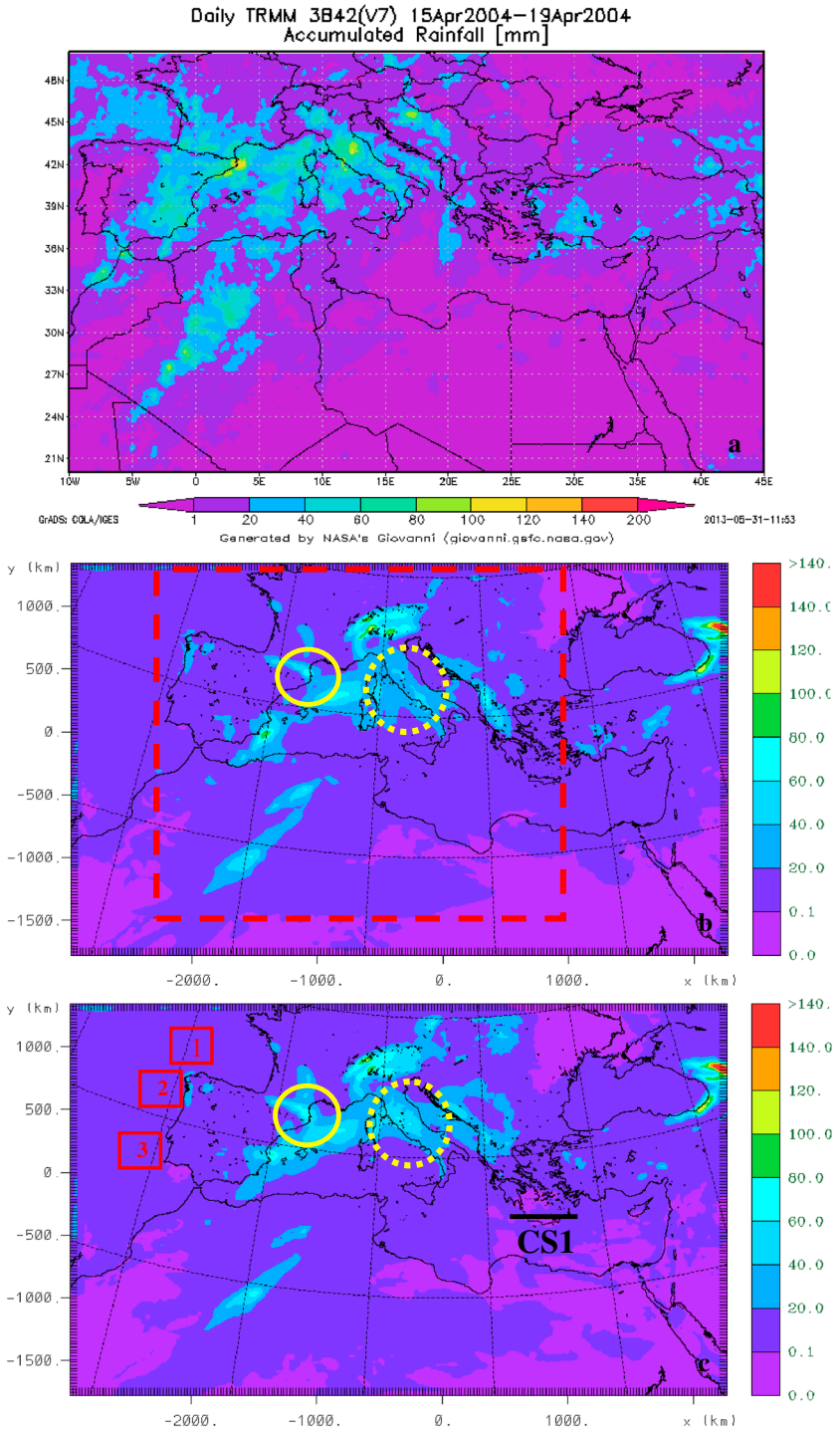

Figure 4.2. Accumulated rainfall (in mm) for the time period 15–19 April 2004 from (a) TRMM, (b) baseline, and (c) RF case. The circles denote the areas where the strongest changes occur due to the inclusion of the dust feedback. The red dashed rectangular refers to the part of the domain with significant amounts of precipitation being affected by the dust cloud. The red numbered boxes indicate areas where sea-salt impact on radiation is calculated and the black CS1 line is the location of the cross section discussed in Figure 7.

underestimation seen over the Iberian Peninsula; however, several improvements are achieved in other regions. As seen in Figure 4.2, the differences are mainly noticed over Italy where the RF case simulates more precisely the accumulated precipitation over Central Italy (Rome) than the baseline simulation which

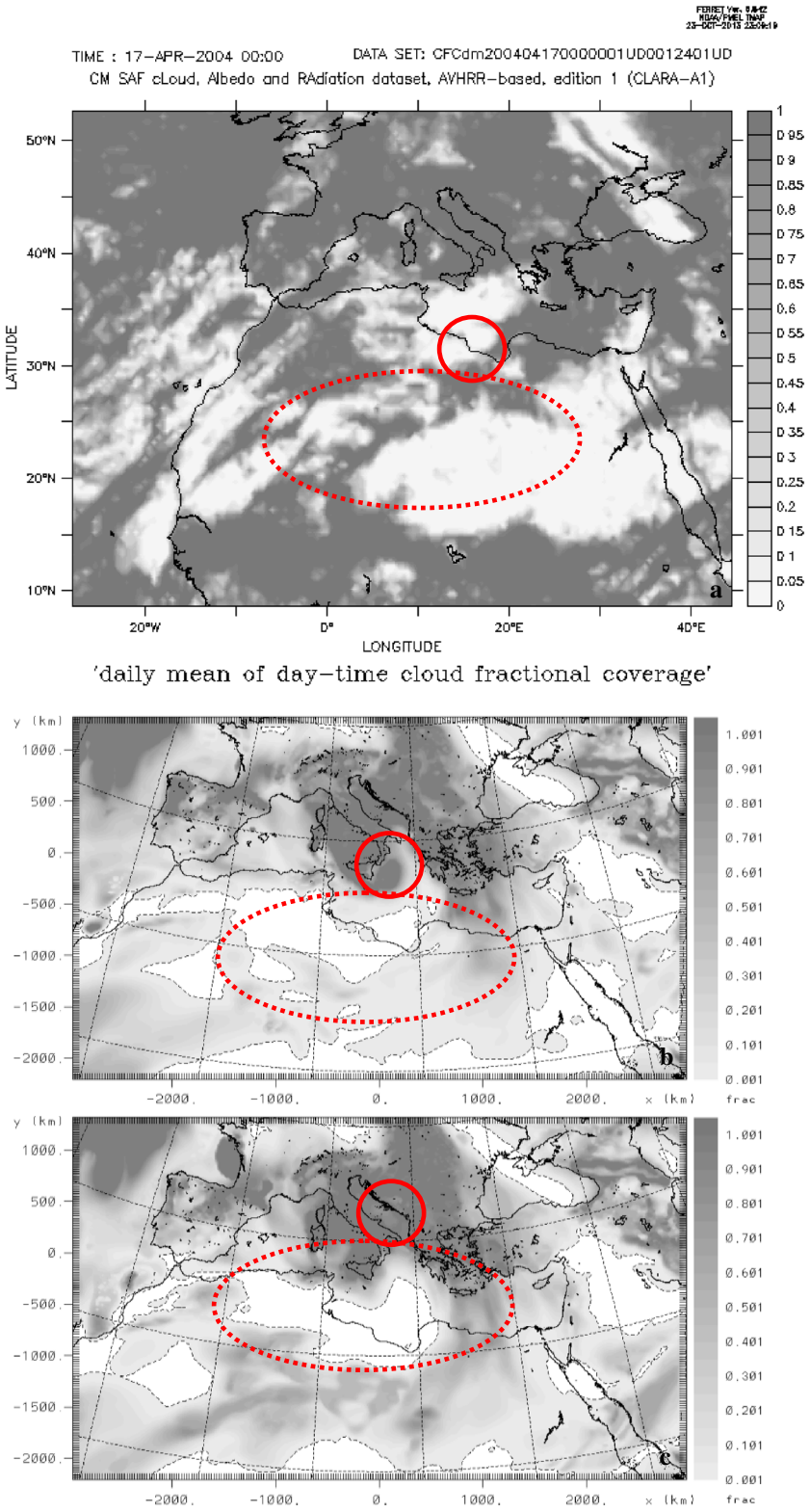

Figure 4.3. (a) Daily mean cloud cover (CC) from CLARA-A1 AVHRR data and modeled CC from (b) the baseline and (c) RF simulation on 17 April 2004, at 12:00 UTC. Circles indicate the most affected areas. Clouds are depicted in grayscale colors and white indicates cloudless areas.

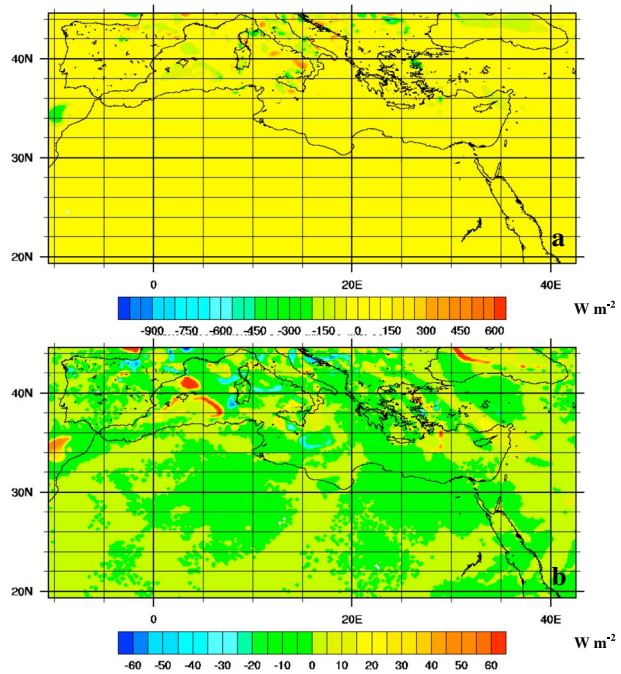

Figure 5. Difference due to the indirect effect in (a) SR and (b) LR expressed as PRFCF − PRF (W m^{-2}) at the first free model layer (P is the respective variable).

underestimates this rainfall event (shown in circles in Figure 4.2). Additionally, the precipitation along the Mediterranean coast of the Iberian Peninsula is closer to TRMM. However, the maximum precipitation is underestimated in both runs probably due to the relatively coarse model resolution. The cloud cover over the Mediterranean region differs between the baseline and RF simulations (Figure 4.3). The direct aerosols effects lead to an altered heat balance and modification of the thermal stratification aloft that, in turn, changes the cloud formation and cloud cover (CC). The main change is a noticeable increase of cloud cover over the North African region and more distant toward the east (shown in circles in Figure 4.3). The formation of cloud over this region is a second parameter, apart from the dust particles, that affects radiation and subsequently other meteorological and chemical parameters, constituting the semidirect feedback mechanism. Another area affected by the inclusion of the radiation impact of dust is south of Italy where a cloud system, stretched south of Sicily in the baseline simulation, in the RF simulation stops inland. The Aqua-AIRS Level-3 cloud cover ascending satellite image confirms the lack of cloud cover in that area.

Separating the direct from the semidirect impact on the radiation fluxes is difficult. However, some features of the semidirect effect can help investigating its relative importance. The semidirect effect is linked to the alteration of the cloud distribution due to changes in the radiation budget. For the semidirect effect to be evident, a main prerequisite must be satisfied: the dust cloud must be collocated in the vicinity of, or travel through, air masses with high water vapor content and/or condensates. The boundary layer over Africa is high during daytime resulting in elevation of the dust cloud over the continent [*Kallos et al*., 1998]. This deep well mixed layer, together with topographic features (mountainous region) may lift dust emissions up to 8 km when the dust cloud reaches the Mediterranean Coast of North Africa. Moving north and eastward the dust cloud travels over areas with enhanced cloud cover, changing the vertical thermal structure and redistributing the condensates. Therefore, the main spatial characteristics of the semidirect effect are the small area of large changes in radiation fluxes and the intensification over areas where the dust cloud and the condensed air masses coexist. Similarly, the perturbations in radiation due to the indirect effect of aerosols can have large values but small spatial extent for both short and longwave radiation (Figures 5a–b). The indirect differences can be the outcome of two mechanisms: alteration of the CCN field and/or mineral dust vertical distribution and a chain effect between these parameters and the radiation budget processes. Regarding T2m, the changes introduced by the indirect effect over Finokalia (TRFCF-TRF) in this case study and at this resolution do not exceed ± 0.2°K since the indirect aerosol effect

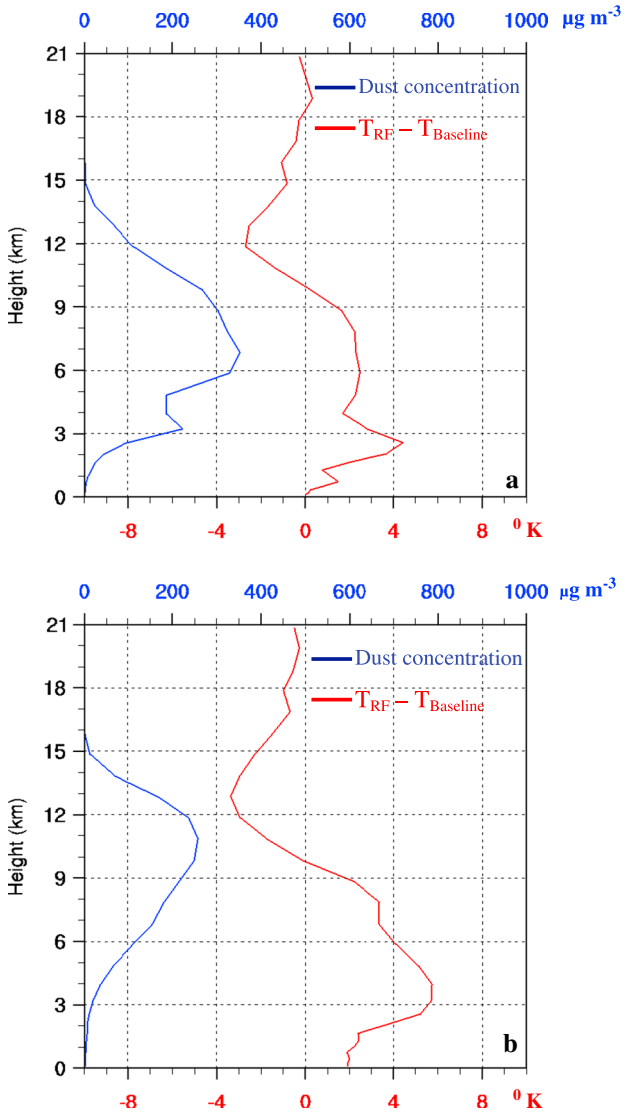

Figure 6. Vertical profile of the absolute difference in temperature (TRF − TBASELINE, in °K red line) and dust concentration (in μg m^{-3} blue line) over Finokalia station (35° 19′ N, 25° 40′ E, altitude 250 m above sea level) on (a) 17 April at 12:00 UTC and (b) 18 April at 12:00 UTC.

for the current simulations is only accounted for by the grid scale clouds (the microphysical module takes into account the prognostic aerosol distribution to compute grid scale cloud properties). Several studies that have assessed aerosol impacts on convective storm systems concluded that they are complex, can have positive or negative forcing, and nevertheless should be investigated on a case-to-case basis [e.g., *van den Heever et al.*, 2006, 2007; *Solomos et al.*, 2011, 2012; *Teller et al.*, 2012].

As discussed, near dust sources where the dust layer is close to the ground, T2m in the RF case is lower compared to the baseline case. However, once moving away from the dust sources and while the dust layer is elevated, the T2m increases with the inclusion of the dust radiative effect. The changes in temperature result from the alterations in the thermal structure (dust particles scattering and absorption) and from the changes in cloud cover. This warmer air over inland Africa and its northerly coast is then transported northeast and reaches Finokalia station where it increases T2m as previously described in this section. Examining the vertical profile of the differences in temperature caused by the impact of dust (Figure 6a), the ΔT2m, expressed as (TRF-TBASELINE), over Finokalia remains positive for an air layer from the surface up to ~8–9 km height that corresponds to the higher dust cloud. The air is warmer below and within the dust layer demonstrating the

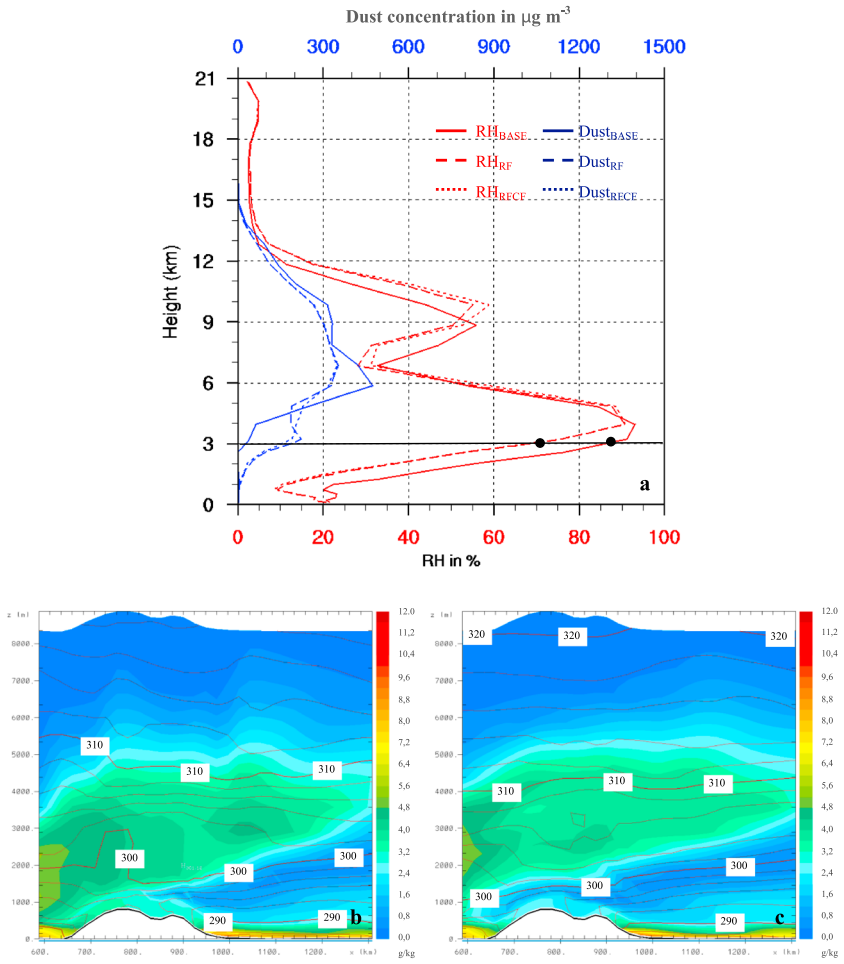

Figure 7. (a) Vertical profile of the relative humidity %RH (red lines) and dust concentration in μg m^{-3} (blue lines) over Finokalia station on 17 April, 12:00 UTC for the three simulations. Water vapor mixing ratio (g kg^{-1}) and theta contours (°K) on a WE cross section over Crete island from (b) baseline and (c) RF simulation on 17 April, 12:00 UTC. The location of the cross section is shown with the black line CF1 in Figure 4.2c.

absorbing character of mineral dust and the trapping of the longwave radiation by the dust layer. The differences in the air temperature on 17 April reach 4.1°K at 2.5 km height.

Above the dust layer the RF simulation gives slightly cooler air masses by ~ −3°K and the perturbation also continues to higher levels but to a smaller extent. On 17 April the dust is distributed over a lower double layer with two peaks. The maximum concentrations of the peaks are 350 μg m^{-3} at 6.5 km and 210 μg m^{-3} at 3 km. On April 18, the dust layer turns into a single higher layer with maximum concentrations of ~280 μg m^{-3} at ~ 9 – 10 km (blue lines in Figure 6). These high dust clouds are not a rare springtime phenomena for the Mediterranean region. As described in *Gobbi et al.* [2000], mineral dust particles can reach and persist for several days at heights of about 10 km. The higher dust cloud of 18 April, even though with less ground level loading (and smaller maximum concentrations) has a larger response on air temperature (Figure 6b). These results indicate that the altitude of the dust layer plays a significant role on the response of the atmosphere to its forcing. Lower dust concentrations that reach higher altitudes can have a similar or larger effect on meteorology than having more dust in lower levels. *Liao and Seinfeld* [1998] have also highlighted that the magnitude of the effect of dust on the radiation budget strongly depends on its altitude.

Moisture vertical profile is also influenced by the changes in the radiation budget. Figure 7a shows the vertical profiles of relative humidity (RH) and dust concentration over Finokalia on 17 April 2004, at 12:00 UTC. The main finding regarding RH consists of a reduction below and within the dust layer when the RF impact is included and an increase of RH at the top of the dust layer (above 9 km). For example at 3 km height the RH of

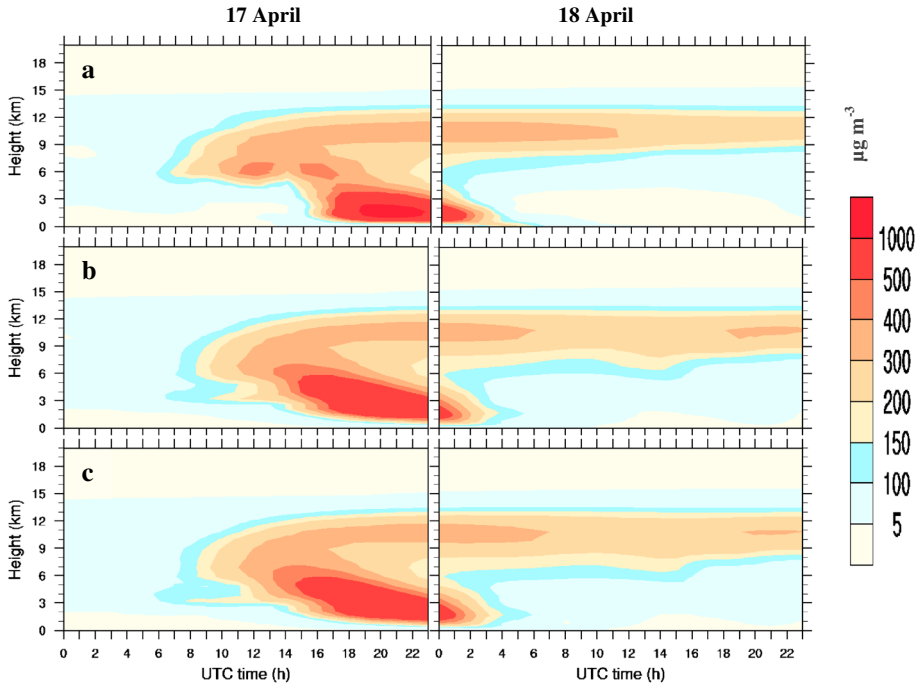

Figure 8. Temporal evolution of the vertical profile of dust concentration ($\mu g\, m^{-3}$) over Finokalia station on (left column) 17 April and (right column) 18 April for (a) baseline, (b) RF, and (c) RFCF simulations.

the baseline simulation is 87% while in the RF run the RH at this height is 70%. This shift persists from 1 km to 4 km height following the lowest dust layer. From 5 km to 7 km, which represents the lowest half of the second dust layer, the RH from the two simulations does not differ. Above 7 km the RH increases in both cases with a higher rate in the RF and RFCF case. The vertical distribution of the water vapor mixing ratio on a WE cross section over Crete Island (Figure 7b for baseline and Figure 7c for RF case) denotes an alteration in the cloud base height which is expected due to the warm and dry air and its increased tendency to rise (the location of the cross section is shown in Figure 4.2c with CS1). The cloud base lifts by approximately 1 km and the potential temperature at the cloud base is 304°K in the RF case (compared to 300°K in the baseline case). It must be noted that in the baseline case the dust layer does not interact in any way with the meteorological parameters, so the changes that result from the inclusion of the feedback mechanisms refer to dust impacts compared to no impact at all.

The inclusion of the feedbacks changes the spatiotemporal characteristics of both dust concentrations (Figure 8) and total condensates (Figure 9) over Finokalia. Regarding dust concentrations, the baseline simulation gives an initially unified dust layer, the bottom of which is located at 5 km on 17 April at noon. The dust layer rapidly descends to 500 m remaining close to the surface until 18 April at 05:00 UTC. The RF simulation gives an initially double dust layer, the bottom of which is located lower than the baseline dust layer (2–3 km) and steadily continues to descend but not below 1 km. During April 18, another higher layer, centered at about 9–10 km, dominates the vertical dust structure in the two cases (baseline and RF/RFCF) indicating long range transport of dust. The radiative feedback and the changes in the thermal structure of the atmosphere result in changes in the wind field. Wind is a central component in dust production and transport, and the dust concentration differences between the baseline and the feedback runs are largely a result of the altered wind field. The inclusion of the CF impact does not have significant impacts on the dust concentration pattern. Similarly, the temporal evolution of the total condensates mixing ratio, averaged over an area of 120 km × 120 km around Finokalia, is shown in Figure 9. The averaging is performed in order to avoid possible biases from potential relocation phenomena. Larger scale relocation is considered a relocation-pattern feedback mechanism. The main difference between the RF (Figure 9b) and baseline (Figure 9a) simulations is the "dry up" of the total condensates (sum of the condensates in all phases) between 3 and 6 km height during the dust event (till 18 April noon hours). The "burn off mechanism of the clouds" is due to the radiative heating of the dust layer, as also described in *Ackerman et al*. [2000]. However, the total condensates during afternoon and the night of April 18th, in the RF case, are larger than in the baseline case indicating an offset of condensates right after the major dust event.

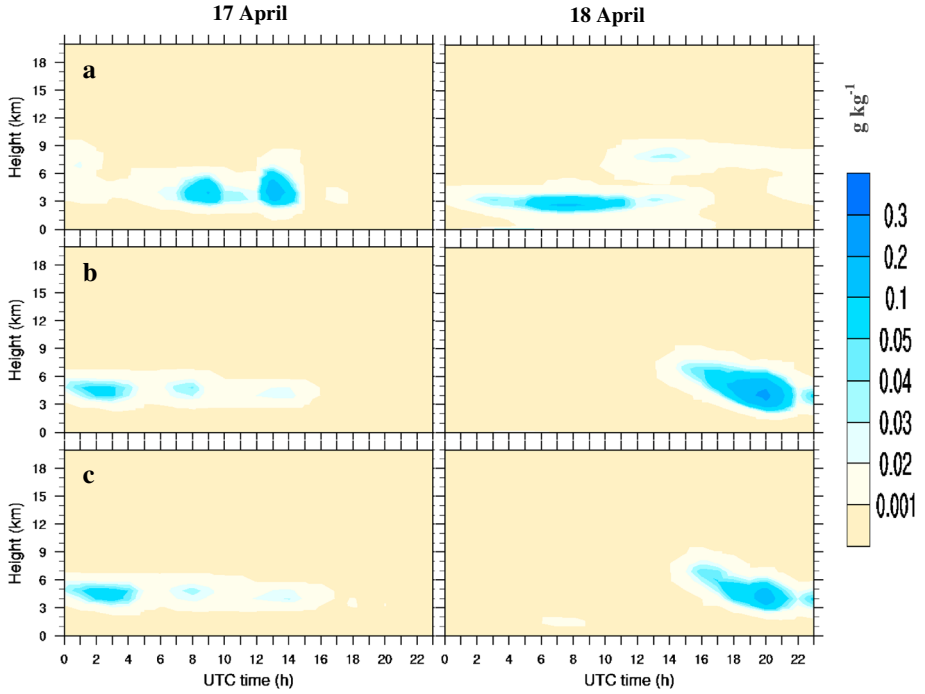

Figure 9. Temporal evolution of the vertical profile of the total condensate mixing ratio (g kg^{-1}) averaged over an area of 120 km × 120 km around Finokalia station on (left column) 17 April and (right column) 18 April for (a) baseline, (b) RF, and (c) RFCF simulations.

During these offset hours the inclusion of the dust indirect effect results in a decrease in magnitude, rather than vertical structure, in the condensate vertical distribution (Figure 9c) that probably results from the increased number of CCN. The activation of the dust particles as CCN is an additional source of cloud droplets relative to the constant CCN background value used in the baseline and RF case. The larger number of CCN competes for less moisture leading to the formation of condensates with smaller diameter that can evaporate more easily.

4.3. Dust Feedback on Photolysis Rates and Ozone

The changes in the solar radiation and temperature have consequences for the photochemical activity and the ozone field over the region. The changes in the ozone distribution may come from the alterations in the photolysis rates, or other factors such as biogenic emissions that increase with temperature. Higher temperatures will generally result in enhanced photochemical activity but lower solar radiation causes a decrease in the actinic fluxes, defining the negative net change in the photolysis rates in cases with high aerosol load. JO1D and shortwave radiation at the surface are indeed lower in the RF simulation than in the baseline simulation and in better agreement with measurements over Finokalia station (Figure 10). The slight but persistent overestimation of the photolysis rates by the model is expected since the model calculates J values taking into consideration all the components of solar radiation (downwelling and upwelling) while the observations are derived from measurements of downwelling radiation fluxes only. *Benas et al.* [2013] defined a mean discrepancy of about 10 – 12% that is consistent with our results. At Finokalia, JNO2 decreases from 11.42 10^{-5} s^{-1} to 8.92 10^{-5} s^{-1} and JO1D from 3.21 10^{-3} s^{-1} to 2.38 10^{-3} s^{-1} from the baseline to the RF simulation. The JO1D vertical profiles reveal that with the inclusion of the dust feedback the surface photolysis rates over Finokalia station decrease near the surface and increase within the dust layer (Figure 11). JNO2 exhibits the same reduction (not shown). The reduction in the photolysis rates due to RF starts from 09:00 UTC and lasts until 13:00 UTC. The relative difference ΔJRF [(JRF − JBASELINE) * 100 / JBASELINE] for O1D reaches −25% near the surface during noon hours on 17 April. The reduction decreases with height up to 1.5 – 2 km where it becomes zero. Above this height the JO1D of the RF simulation becomes larger than the JO1D of the baseline simulation (ΔJRF becomes positive) by approximately 4 – 5%. The reduction comes as a result of both the direct reduction in SR from dust and the alteration in the radiation budget from the changes in cloud cover. The inclusion of the indirect effect (RFCF case) further alters the vertical profile of the J values (the total difference ΔJRFCF is expressed as (JRFCF − JBASELINE) * 100 / JBASELINE). On 17 April,

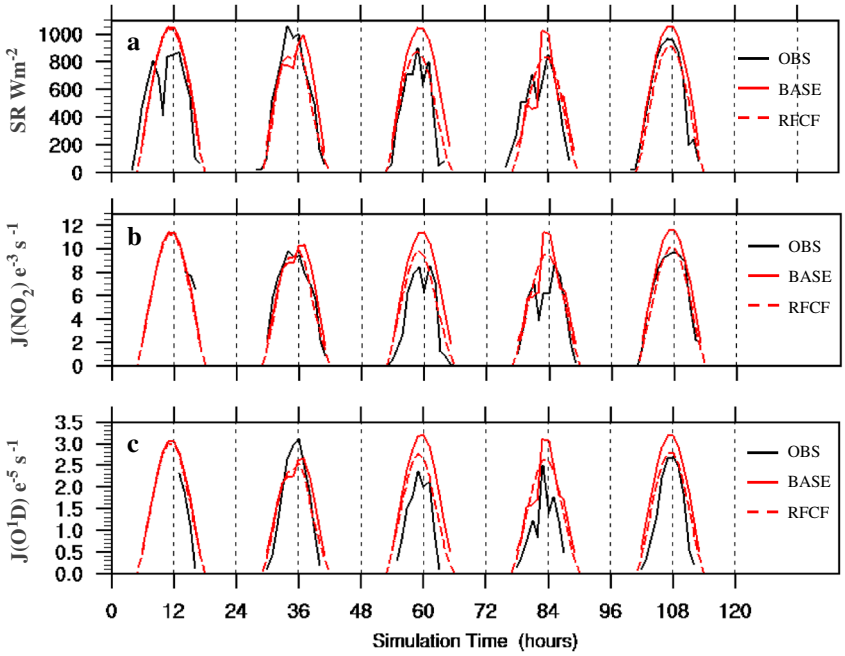

Figure 10. (a) Shortwave radiation in the first model layer (W m^{-2}) and photolysis rates of (b) NO2 (1e−3 s^{-1}) and (c) O1D (1e−5 s^{-1}) as a function of forecast hour (120 h from 15 to 19 April 2004) compared with measurements from the Finokalia station, Crete (35° 19′ N, 25° 40′ E, 250 m above sea level). Black lines: measurements. Red continuous lines: baseline case. Red dashed lines: RFCF case.

the inclusion of the indirect effect reduces the JO1D near the surface even further with ΔJRFCF reaching −30% in comparison to ΔJRF of −25%.

Several sensitivity tests are also performed in order to investigate the corresponding reduction at the surface in SR and J-values as a function of AOD. For this purpose, six additional simulations were performed for the RF

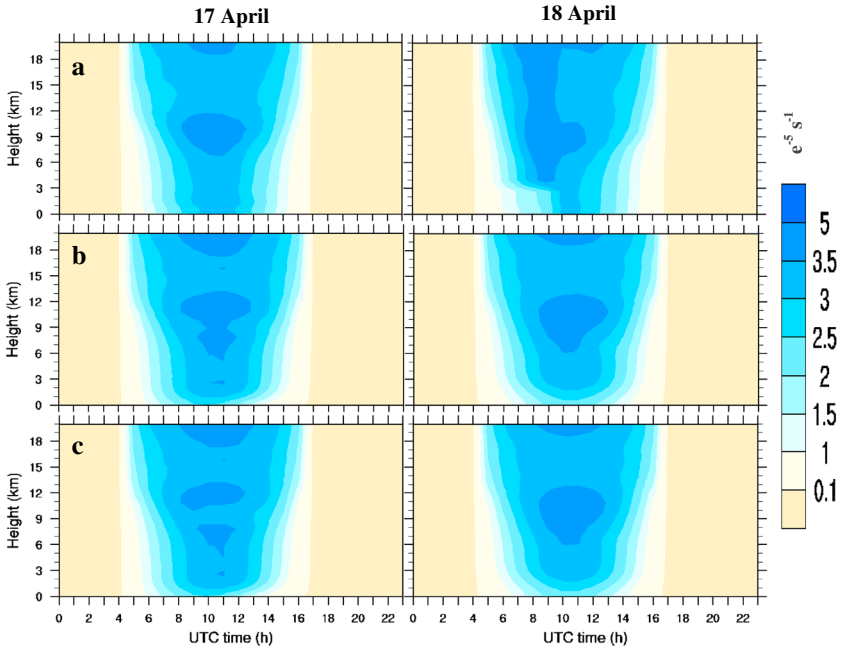

Figure 11. Temporal evolution of the vertical profile of JO1D (e−5 s^{-1}) over Finokalia station on (left plots) 17 April and (right plots) 18 April for the (a) baseline, (b) RF, and (c) RFCF simulation.

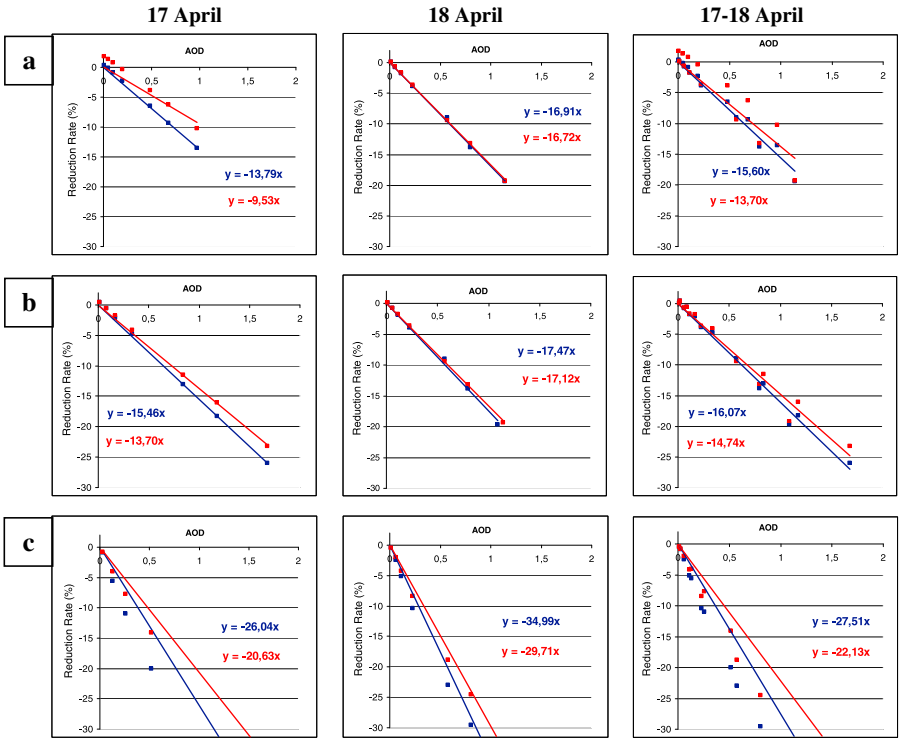

Figure 12. Reduction (in %) of shortwave radiation (ΔS) and photolysis rates (ΔJO1D) at the surface as a function of AOD (for Finokalia station) at 09:00 UTC (upper row), (middle row) 12:00 UTC and (lower row) 15:00 UTC. Left plots refer to 17 April, middle plots refer to 18 April, and right plots to both days 17 and 18 April. The grey lines are for ΔJ and the black lines for ΔS.

case, for 17 to 18 April to assess the role of different dust cloud structures, where the AOD profile of the RF case is multiplied by a factor (f) (i.e., 0.015, 0.07, 0.15, 0.3, 0.7, and 1.4) to represent different "strengths" of the same dust event. The changes (ΔS and ΔJ, respectively, for SR and J-values) are expressed as the percentage (PRFf − PBASELINE)*100% / PBASELINE, where PRFf are the parameter values (SR and J) from the respective sensitivity test with the multiplying factor f (Figure 12). The ΔS are negative except for very low AOD (~ 0.01) where a slight increase is observed. This is evident on 17 April at 09:00 and 12:00 UTC when the dust cloud is composed of two layers. On 17 April 15:00 and during 18 April, when the dust cloud turns into a single layer, the changes in SR and J-values under low AOD are negative. The positive ΔS for very low AOD during 17 April is a result of the photon path length increase due to multiple scattering (two dust layers). In detail, it must be noted that the shortwave radiation parameter from the model refers to direct and diffuse radiation fluxes in the 200–3846 nm band and thus not direct solar radiation alone. The positive ΔS in low AOD indicates that the increase in the diffuse component of the shortwave radiation caused by the aerosols may overcome the decrease in the direct component. Therefore, the slight increase in the total (direct and diffuse) solar radiation under low AOD is the net effect of the two opposite-sign feedbacks on direct and diffuse shortwave fluxes separately.

The photolysis rates have a smoother slope of reduction than the SR (Figure 12, lower plots) due to the fact that the photolytic reactions occur in a subpart of the SR wavelength band. The changes in J-values follow the reduction of SR relatively closely during morning and noon hours, especially on 18 April when the dust exhibited a single layer structure. Both ΔJ and ΔS are more strongly reduced during the afternoon than at noon and morning hours. The reduction varies from 15.6% to 31.3% for SR and from 13.7% to 24.9% for J-values showing a linear relationship in all cases. The reductions on 18 April for all hours are larger than those on 17 April when the dust load is larger but the dust cloud is located at lower altitudes. This corroborates the significance of altitude of the aerosol layer in assessing its radiative effects. When adding all the results obtained from the sensitivity tests, during different hours that refer to different dust vertical distributions (height, layering, concentrations, etc), the total reduction rate is 22.5% for SR and 18.8% for J-values. The endpoint results of this linear relation are in good agreement with the observational results of *Gerasopoulos et al.* [2012] who mentioned less than 6% reduction in photolysis rates for background conditions and 30 – 40% reductions during

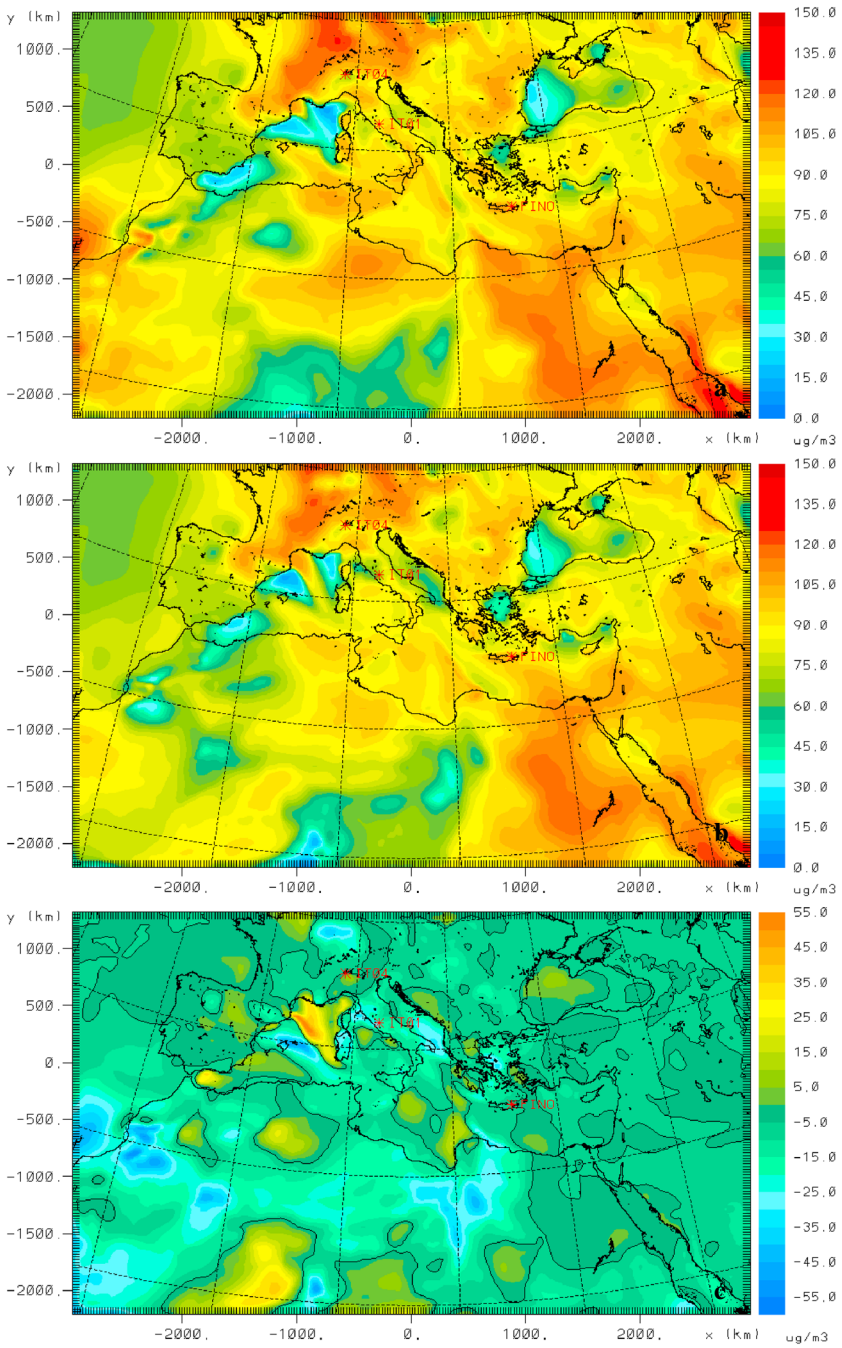

Figure 13. Ozone concentrations in μg m^{-3} from (a) baseline and (b) RFCF simulation and (c) the difference expressed as CRFCF − CBASELINE on 17 April 2004 at 12:00 UTC.

dust events with an AOD above 1.5. However, significant differences within the ±10% range in the reduction rate are introduced (i.e., an AOD of 0.8 during 09:00 UTC can give a reduction of 13% and during afternoon hours the same AOD leads to a decrease in J-values by 24%; according to the linear regression a reduction of ~ −16% is expected underlining the significance of solar zenith angle).

The impact of dust on the photolysis rates is also reflected in the ozone concentrations over the affected area. The consequent ozone response to the changes in the photolytic frequencies depends on the NOx and VOC availability over the area of interest [*Stockwell and Goliff*, 2004]. *Murazaki and Hess* [2006] suggested that higher photochemical rates over regions with low pollution result in ozone reduction because destruction dominates

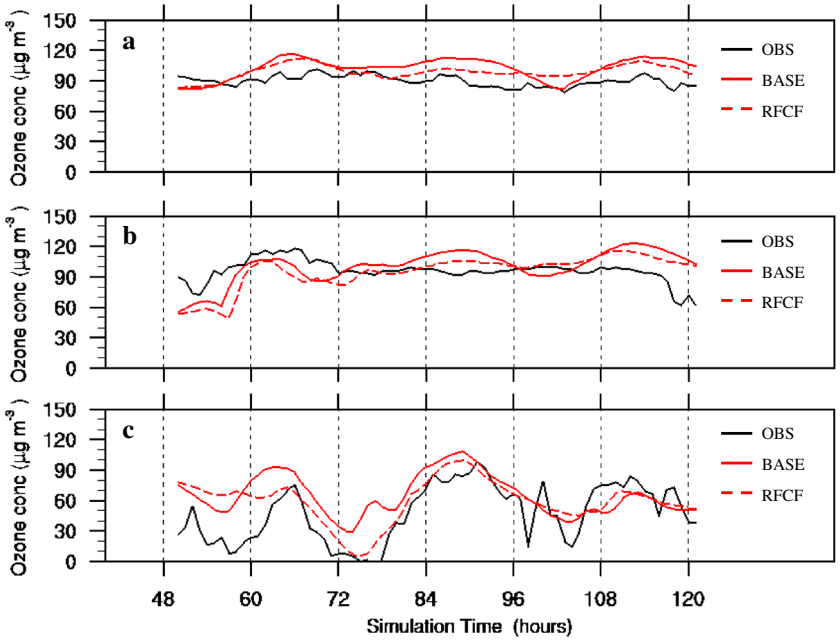

Figure 14. Time series of ozone concentrations in $\mu g\ m^{-3}$ (48 to 120 forecast hours from 17 to 19 April 2004) compared with measurements: (a) Finokalia station, Greece (35° 19′ N, 25° 40′ E), (b) Akrotiri station, Greece (35° 32′ N, 24° 03′ E), and (c) Montelibretti station, Italy (42° 06′ N, 12° 38′ E). Black lines refer to measurements, red continuous lines to the model results from the baseline case, and the red dashed lines to the RFCF case.

the chemistry of ozone. Accordingly, over regions with low anthropogenic pollution low photolysis rates indicate low activity. Therefore, the destruction of ozone is performed at a lower rate whilst the production is limited due to low levels of NOx and VOC, leading to a longer residual of ozone in the area (shown in black circle in Figure 13). ΔC expressed as CRFCF − CBASELINE reaches $50\ \mu g\ m^{-3}$ over Africa and the south coast of France. Differences of ~ −20 to $-40\ \mu g\ m^{-3}$ are noted over Lybia and the west coast of Africa as well as between or downwind of areas where a ΔC is positive. Our results are in agreement with previous studies that found nonmonotonous changes in the ozone concentrations depending on the pollution level at the area of interest [*Fast et al.*, 2006; *Forkel et al.*, 2012]. This pattern may be explained by the requirement-availability rule that is valid for the ozone cycle and its precursors. Another reason is the establishment of a well-mixed layer that is formed from the warm and dry air moving across the desert that leads to ozone dilution into a deeper layer and lower surface concentrations. Finokalia, Akrotiri, and Montelibretti stations are affected by the dust layer and the ozone concentrations over these stations are altered by the inclusion of the dust feedback (Figure 14). The results from the RF simulation are similar to RFCF. Finokalia and Akrotiri are stations mainly affected by long range transport of pollution indicated by the lack of a clear diurnal cycle of ozone. Montelibretti station exhibits clear production-loss patterns in the daily variation of ozone concentrations mainly attributed to its location near areas with high precursors concentrations. In general, ozone concentrations over these stations are decreased in the RF case compared to the baseline case, giving better agreement with observed values. During ozone buildup hours, the absolute difference in the ozone concentrations over Finokalia and Akrotiri reaches $10\ \mu g\ m^{-3}$ that is a decrease of about 8–10% with respect to the baseline run. The difference for Montelibretti, however, is much larger, reaching $40\ \mu g\ m^{-3}$ that is probably related to the location of this station (closer to industrial and urban areas) compared to Finokalia and Akrotiri stations. The decrease in ozone in the RF simulation may additionally be the result of the deeper mixed layer that results from the warm and dry air masses in the area. The current sensitivity tests thus indicate the significance of the dust impact on photolysis rates in the East Mediterranean Region. Including dust links with solar radiation is an important process with a number of complex feedbacks that should be taken into consideration in atmospheric chemistry studies in this region.

4.4. Impact of Sea-Salt Aerosols

Sea-salt particles (SS) are produced as a result of the wind effect on the surface of the water body and are characterized as primary emissions. SS aerosol has mainly scattering properties in the shortwave bands and is

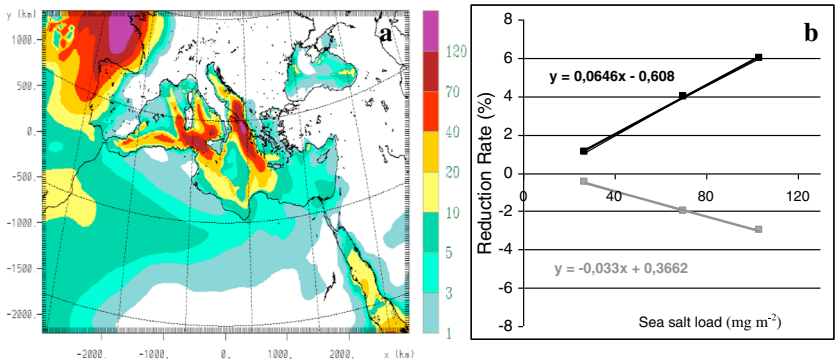

Figure 15. (a) Sea-salt total column load (mg m^{-2}) from the RFCF simulation. (b) Changes (%) in shortwave radiation (gray line) and downwelling longwave radiation (black line) at the surface expressed as (RRF_SS − RBASELINE)*100 / RBASELINE (where R is the SR or LR) as a function of sea-salt total column load.

the major cause of light scattering in clean marine conditions [*Quinn and Bates*, 2005]. Two additional sensitivity tests are performed activating the SS-radiation interaction: including only sea salt (RF_SS simulations) and adding SS to mineral dust particles (RF_MDSS). The single scattering albedo for all the aerosol modes (ω) in each band, when more than one aerosol type is included, is calculated by weighting the single scattering albedo of each aerosol mode *i* as follows:

$$\omega(\lambda) = \frac{1}{b(\lambda)} \sum_{i=1}^{N} \varpi_i(\lambda) \cdot b_i(\lambda) \tag{4}$$

The asymmetry parameter (*g*) for the whole aerosol distribution is given as:

$$g(\lambda) = \frac{1}{b_s(\lambda)} \sum_{i=1}^{N} \overline{g}_i(\lambda) \cdot b_{s_i}(\lambda) \tag{5}$$

where *b* and b_s are, respectively, the extinction and the scattering coefficients. The band- and mode-dependent ωi and *gi* are derived from the Mie calculations.

SS particles are present over the Mediterranean Sea and the Atlantic Ocean with total column loads varying from 10 to 100 mg m^{-2} (Figure 15a). The attenuation in SR due to SS particles is much smaller than that of the mineral dust during this test event, where soil dust dominates the aerosol load in the atmosphere. SS alone exhibits mainly characteristics of the semidirect effect and, when combined with mineral dust, SS enhances the dust negative radiative forcing. It is difficult to identify the SS direct effect since the areas where these particles are present, in this test case, coincide with areas with increased condensates load and/or dust. For this reason the RF_SS simulation was performed to define a region with SS and no condensates load (mineral dust is not activated in the radiation module). Such areas are found along the Atlantic coast of northern Spain (box 1 in Figure 4.2c) and Portugal (boxes 2 and 3 in Figure 4.2c). Oceanic areas are chosen since areas with relatively lower albedo exhibit a more evident radiative effect as described in *Lundgren et al.* [2013]. For a total column SS load of ~ 110 mg m^{-2} over area 1, the reduction in the SR during noon hours, expressed as (SRRF_SS − SRBASELINE)*100 / SRBASELINE is ~ 3% while LR increases by ~ 6% with the inclusion of the SS impact. In area 2 there is a reduction of −2% in SR and an increase of 4% in LR when the total column salt load reaches 70 mg m^{-2}. While in area 3, an SS load of ~ 27 mg m^{-2} causes a reduction of −0.5% in the SR and an increase in the LR of ~ 1.1%. These results indicate that the reduction in SR and the increase in LR correspond linearly to the sea-salt load. SR reduces at almost half (−3.3%) the rate of enhancement of LR (+ 6.5%) per 100 mg m^{-2} sea-salt load (Figure 15b). *Li et al.* [2008] also found an almost linear dependence of the radiative budgets on the sea-salt loading. A vertical profile of the sea-salt concentration over Atlantic Ocean and Mediterranean Sea shows that these particles have the same vertical distribution (not extending above 2 km) over both areas. Therefore, since the vertical profile of the sea-salt particles can be expected to be similar, it may be assumed that these alteration results are also applicable to the Mediterranean Sea, under cloud- and dust-free conditions, where the sea-salt load varies between 10 and 70 mg m^{-2}. These differences in the radiation fluxes are much smaller than the ones discussed in paragraph 4.1

for mineral dust during dust storm events. However, sea-salt particles have a more frequent presence in the region compared to dust, which is mainly an episodic pollutant, making the SS contribution small though more persistent.

In order to quantify the impact of the different types of aerosols on precipitation, separately and in a mixture, the precipitation over the subdomain indicated with the red dashed box in Figure 4.2b is assessed. This is an area with significant precipitation impacted by the presence of dust and sea salt. The total precipitation integrated over the entire subdomain (Subdomain Total Precipitation — STP) does not exhibit large differences between runs where only the interaction of the aerosols with the radiation is activated (Table 3). These results indicate that the presence of aerosols, in terms of radiative forcing, cannot change the total precipitated water over the area of interest for the five-day period. However, the inclusion of the cloud forcing (RFCF simulation) has a larger effect on precipitation by increasing the STP by ~3% from the baseline to the RFCF case. Even though STP in the RFCF cases is larger, the inclusion of the cloud forcing decreases the precipitation maxima values. On a day-to-day basis the inclusion of the aerosol impact on radiation seems to result in a suppression of daily subdomain total precipitation (DSTP) during the day of the major event (17 April and to a lesser extent 18 April) and an enhancement of the DSTP loads after 48 h (19 April). The DSTP on 17 April decreases from 23,150 mm d^{-1} in the baseline case to 20,700 mm d^{-1} in the RF case while an increase is noted on 19 April from 26,300 mm d^{-1} in the baseline case to 31,900 mm d^{-1} in the RF case. Maximum daily precipitation (MDP) exhibits the same feedback reaction with maximum changes noticed when the indirect effect is activated. On 17 and 18 April MDP rates are 39.48 mm d^{-1} and 49.66 mm d^{-1} in the baseline simulation and 31.49 mm d^{-1} and 42.43 mm d^{-1} in the RF_MDSS simulation representing a decrease of about 20% (17 April) and 14% (18 April). The precipitation on 19 April seems to make up for the suppression of the previous days by increasing MDP from 53.56 mm d^{-1} in the baseline simulation to 64.85 mm d^{-1} in the RF_MDSS simulation. Sea salt alone also affects precipitation field; however, its contribution is smaller than mineral dust. These results indicate that, domain wide, activating natural particles as CCN can affect precipitation more significantly than altering the radiation budget. A suppression of precipitation is evident on the days of the major event and a compensation is noticed on the following day, leading to no major changes on domain total precipitation over the whole precipitating period.

5. Concluding Remarks

The scope of this work has been to investigate and assess the mesoscale effects of natural aerosols on the radiation and improve our understanding on the feedback mechanisms that influence the meteorological fields and atmospheric chemistry parameters, using a fully coupled model. The inclusion of the direct, semidirect, and indirect effects of desert dust and sea-salt particles leads to the improvement of the model simulations and corroborates the positive/negative influence of each aerosol type as well as their combination. In general, mineral dust and sea salt affect the atmospheric conditions over the Mediterranean Region due to their frequent, either episodic or constant, presence. The results from this investigation are summarized below.

Natural aerosols direct and semidirect effects are assessed by an online treatment of the aerosol impact on the radiation fluxes:

1. Mineral dust abundance in the atmosphere leads to a reduction in the shortwave radiation and an increase in the downwelling longwave radiation at noon, as expected, with a respective change of ~ −75 W m^{-2} and 40 W m^{-2} per unit dust loading (in g m^{-2}). The upwelling longwave radiation exhibits a daytime reduction and a nighttime increase.
2. Sea-salt particles net effect is similar, in sign, to the dust effect described above, but the relative contribution is much smaller than that of dust particles.
3. The semidirect effect is more noticeably remote from the aerosol sources. The conditions for the semidirect effect to be evident are that dust cloud altitude exceeds 2–3 km and dusty air masses travel through moist air. The semidirect effect can lead to large changes in the radiation budget, due to altered cloud formation/distribution.

The feedback of natural aerosols on meteorological parameters is assessed by including both direct and indirect effects (prognostic aerosol distribution in the explicit cloud nucleation scheme):

1. The air temperature, below and within the dust layer, increases with the inclusion of the dust impact on radiation, with the direct effect being stronger than the indirect. The warmer air leads to a cloud base lifting and a dry out of condensates.
2. Changes in the precipitation patterns are also noted over areas affected by the aerosol radiative impact. During the intense dust event the aerosols suppress precipitation. On subsequent days, however, the precipitation increases, showing that the inclusion of the aerosol radiative effects does not change the total precipitation at the end of the event. The indirect effect is larger but does not exceed a 3% increase in total precipitated water. However, the aerosol impact on small-scale convective clouds is not assessed due to the model resolution.

Aerosol feedbacks on photochemical production are assessed through the inclusion of all processes mentioned above:

1. The reduction in J-values results from the reduction in shortwave radiation due to the direct attenuation from the dust particles and the increase in cloud cover.
2. The reduction of the J-values at the surface are larger when the dust cloud is a single layer located higher in the atmosphere than when it is located in lower altitudes, even though the dust load may be higher. These results indicate that higher dust clouds can have larger impact on surface shortwave radiation and photochemistry.
3. The ozone concentrations in the area are also altered by the inclusion of the aerosol impact. The comparison with measurements shows that the model performance regarding ozone concentrations is improved. In general, the ozone concentrations are reduced, following the reduction in the photolysis rates, influenced by ozone precursor emissions. An O3 reduction is also noted over major parts of Africa that are far from emissions sources. The reason for the reduction in ozone concentrations in this area is the deeper mixed layer that results from the warmer air masses.
4. However, the ozone concentrations increase near dust sources when the impact of aerosols on radiation is taken into account. This is the result of the lower photolysis rates (both JNO2 and JO1D) that reduce destruction of ozone. The low destruction rates contribute to the persistence of ozone over areas with low precursor concentrations, such as the areas near dust sources.

The sensitivity tests performed to assess the magnitude of reduction in shortwave radiation and photolysis rates under different conditions reveal that the attenuation of both parameters can be characterized as linear for separate times of the day. The reduction of both shortwave radiation and J-values is significantly larger during afternoon hours compared to morning and noon hours. The rate of reduction is also higher when the dust cloud is located at higher altitudes and consists of a single layer. Therefore, AOD is not sufficient to describe the impact of aerosols on radiation and photodissociation rates. Solar zenith angle and the vertical structure of the aerosol layer also play a significant role.

Our results highlight the significance of including the impact of aerosols on radiation and clouds in air quality regional studies and weather forecasting systems. Biases in several meteorological components and air quality parameters can be introduced if these links and feedbacks are not incorporated into the modeling systems.

Acknowledgments

This work has been supported by the European Union 6th Framework Program CIRCE IP, contract 036961 and the EUROCONTROL Research Studentship Agreement CO6/22048ST. The research has also received funding from the European Research Council under the European Union's 7th Framework Programme (FP7/2007–2013) / ERC grant agreement 226144. Special thanks to the National Observatory of Athens (Evangelos Gerasopoulos) and the University of Crete, Department of Chemistry (Prof. Nikos Mihalopoulos, Prof. Mihalis Lazaridis, and Dr Giorgos Kouvarakis) for providing the necessary observations from the Finokalia, Akrotiri, and Heraklion stations. The images and data used in this study were acquired using the GES-DISC Interactive Online Visualization ANd aNalysis Infrastructure (Giovanni) as part of the NASA's Goddard Earth Sciences (GES) Data and Information Services Center (DISC). The work related to clouds was done by using data from EUMETSAT's Satellite Application Facility on Climate Monitoring (CM SAF) and their product version http://dx.doi.org/10.5676/EUM_SAF_CM/CLARA_AVHRR/V001 DOI:10.5676/EUM_SAF_CM/CLARA_AVHRR/V001#_blank#EUM_SAF_CM/CLARA_AVHRR/V001.

References

Ackerman, A. S., O. B. Toon, D. E. Stevens, A. J. Heymsfield, V. Ramanathan, and E. J. Welton (2000), Reduction of tropical cloudiness by soot, *Science*, *288*, 1042–1047.

Albers, S., J. McGinley, D. Birkenheuer, and J. Smart (1996), The Local Analysis and Prediction System (LAPS): Analysis of clouds, precipitation and temperature, *Weather Forecast.*, 273–287.

Andreae, M. O., and D. Rosenfeld (2008), Aerosol–cloud–precipitation interactions. Part 1. The nature and sources of cloud-active aerosols, *Earth Sci. Rev.*, *89*, 13–41.

Astitha, M., and G. Kallos (2008), Gas-phase and aerosol chemistry interactions in South Europe and the Mediterranean Region, Special Issue on "Physics-Chemistry Interactions from the Air Quality Perspective" *Env. Fluid Mechanics*.

Bangert, M., C. Kottmeier, B. Vogel, and H. Vogel (2011), Regional scale effects of the aerosol cloud interaction simulated with an online coupled comprehensive chemistry model, *Atmos. Chem. Phys.*, *11*, 4411–4423, doi:10.5194/acp-11-4411-2011.

Barahona, D., and A. Nenes (2009), Parameterizing the competition between homogeneous and heterogeneous freezing in ice cloud formation - polydisperse ice nuclei, *Atmos. Chem. Phys.*, *9*, 5933–5948.

Benas, N., E. Mourtzanou, G. Kouvarakis, A. Bais, N. Mihalopoulos, and I. Vardavas (2013), Surface ozone photolysis rate trends in the Eastern Mediterranean: Modeling the effects of aerosols and total column ozone based on Terra MODIS, *Atmos. Environ.*, *74*, 1–9l, doi:10.1016/j.atmosenv.2013.03.019.

Bian, H., M. J. Prather, and T. Takemura (2003), Tropospheric aerosol impacts on trace gas budgets through photolysis, *J. Geophys. Res.*, *108*(D8), 4242, doi:10.1029/2002JD002743.

Binkowski, F. S., and U. Shankar (1995), The regional particulate matter model, 1. model description and preliminary results, *J. Geophys. Res.*, *100*, 26,191–26,209.
Binkowski, F. S., and S. J. Roselle (2003), Models-3 Community Multiscale Air Quality (CMAQ) model aerosol component 1. Model description, *J. Geophys. Res.*, *108*(D6), 4183, doi:10.1029/2001JD001409.
Carter, W. P. L. (2000), Implementation of the SAPRC-99 chemical mechanism into the models-3 framework, Report to the United States Environmental Protection Agency.
Carter, W. P. L., C. G. Sauer, D. R. Fitz, K. Bumiller, C. Bufalino, I. Malkina, J. T. Pisano, M. Smith, and D. R. Cocker III (2003), A new environmental chamber facility for atmospheric chemical mechanism evaluation, Presented at the Gordon Conference on Atmospheric Chemistry, Big Sky Resort, Montana, September 7-12.
Castro, T., S. Madronich, S. Rivale, A. Muhlia, and B. Mar (2001), The influence of aerosols on photochemical smog in Mexico City, *Atmos. Environ.*, *35*, 1765–1772.
Cotton, W. R., et al. (2003), RAMS 2001: Current status and future directions, *Meteorol. Atmos. Phys.*, *82*, 5–29, doi:10.1007/s00703-001-0584-9,2003.
DeMott, P. J., K. Sassen, M. Poellot, D. Baumgardner, D. C. Rogers, S. Brooks, A. J. Prenni, and S. M. Kreidenweis (2003), African dust aerosols as atmospheric ice nuclei, *Geophys. Res. Lett.*, *30*(14), 1732, doi:10.1029/2003GL017410.
Dickerson, R., S. Kondragunta, G. Stenchikov, K. Civerolo, B. Doddridge, and B. Holben (1997), The impact of aerosol on solar UV radiation and photochemical smog, *Science*, *278*, 827–830.
Engel, A., et al. (2006), Highly resolved observations of trace gases in the lowermost stratosphere and upper troposphere from the SPURT project: An overview, *Atmos. Chem. Phys.*, *6*, 283–301.
Fast, J. D., W. I. Gustafson, R. C. Easter, R. A. Zaveri, J. C. Barnard, E. G. Chapman, G. A. Grell, and S. E. Peckham (2006), Evolution of ozone, particulates, and aerosol direct radiative forcing in the vicinity of Houston using a fully coupled meteorology-chemistry-aerosol model, *J. Geophys. Res.*, *111*, D21305, doi:10.1029/2005JD006721.
Fischer, H., M. Lawrence, C. Gurk, P. Hoor, J. Lelieveld, M. I. Hegglin, D. Brunner, and C. Schiller (2006), Model simulations and aircraft measurements of vertical, seasonal and latitudinal O3 and CO distributions over Europe, *Atmos. Chem. Phys.*, *6*, 339–348.
Forkel, R., J. Werhahn, A. B. Hansen, S. McKeen, S. Peckham, G. Grell, and P. Suppan (2012), Effect of aerosol-radiation feedback on regional air quality a case study with WRF/Chem, *Atmos. Environ.*, *53*, 202–211.
Forster, P., et al. (2007), Changes in atmospheric constituents and in radiative forcing, in *Climate Change 2007: The Physical Science Basis. Contribution of Working Group I to the 4th Assessment Report of the IPCC*, Cambridge Univ. Press, Cambridge, United Kingdom and New York, USA.
Fountoukis, C., and A. Nenes (2005), Continued development of a cloud droplet formation parameterization for global climate models, *J. Geophys. Res.*, *110*, D11212, doi:10.1029/2004JD005591.
Gerasopoulos, E., G. Kouvarakis, M. Vrekoussis, C. Donoussis, M. Kanakidou, and N. Mihalopoulos (2006), Photochemical ozone production in the Eastern Mediterranean, *Atmos. Environ.*, doi:10.1016/j.atmosenv.2005.12.061.
Gerasopoulos, E., P. Kokkalis, V. Amiridis, E. Liakakou, C. Pérez, K. Haustein, K. Eleftheratos, M. O. Andreae, T. W. Andreae, and C. S. Zerefos (2009), Dust specific extinction cross-sections over the Eastern Mediterranean using the BSC-DREAM model and sun photometer data: The case of urban environments, *Ann. Geophys.*, *27*, 2903–2912, doi:10.5194/angeo-27-2903-2009.
Gerasopoulos, E., S. Kazadzis, M. Vrekoussis, G. Kouvarakis, E. Liakakou, N. Kouremeti, D. Giannadaki, M. Kanakidou, B. Bohn, and N. Mihalopoulos (2012), Factors affecting O3 and NO2 photolysis frequencies measured in the eastern Mediterranean during the five-year period 2002–2006, *J. Geophys. Res.*, *117*, D22305, doi:10.1029/2012JD017622.
Gobbi, G. P., F. Barnaba, R. Giorgi, and A. Santacasa (2000), Altitude-resolved properties of a SaharanDust event over the Mediterranean, *Atmos. Environ.*, *34*, 5119–5127.
Gong, S. L. (2003), A parameterization of sea-salt aerosol source function for sub- and super-micron particles, *Global Biogeochem. Cycles*, *17*(4), 1097, doi:10.1029/2003GB002079.
Grell, G., and A. Baklanov (2011), Integrated modeling for forecasting weather and air quality: A call for fully coupled approaches, *Atmos. Environ.*, doi:10.1016/j.atmosenv.2011.01.017.
Guenther, A., et al. (1995), A global model of natural volatile organic compound emissions, *J. Geophys. Res.*, *100*(D5), 8873–8892.
Haywood, J., and O. Boucher (2000), Estimates of the direct and indirect radiative forcing due to tropospheric aerosols: A review, *Rev. Geophys.*, *38*(4), 513–543.
Helmert, J., B. Heinold, I. Tegen, O. Hellmuth, and M. Wendisch (2007), On the direct and semi-direct effect of Saharan dust over Europe: A case study, *J. Geophys. Res.*, *112*, D13208, doi:10.1029/2006JD007444.
Hertel, O., R. Berkowicz, J. Christensen, and O. Hov (1993), Test of two numerical schemes for use in transport – chemistry models, *Atmos. Environ.*, *27A*, 2591–2611.
Hess, M., P. Koepke, and I. Schult (1998), Optical properties of aerosols and clouds: The software package OPAC, *Bull. Am. Meteorol. Soc.*, *79*, 831–844.
Iacono, M. J., Delamere, J. S., Mlawer, E. J., Shephard, M. W., Clough, S. A., and Collins, W. D. (2008), Radiative forcing by long-lived greenhouse gases: Calculations with the AER radiative transfer models, *J. Geophys. Res.*, *113*, D13103, doi:10.1029/2008JD009944.
Intergovernmental Panel on Climate Change (IPCC) (2007), Changes in atmospheric constituents and radiative forcing, in *Climate Change 2007: The Physical Science Basis*, Cambridge Univ. Press, New York, USA, and Cambridge, U. K.
Jacobson, M. Z. (1997), Development and application of a new air pollution modeling system, Part III: Aerosol-phase simulations, *Atmos. Environ.*, *31A*, 587–608.
Jacobson, M. Z. (1998), Studying the effects of aerosols on vertical photolysis rate coefficient and temperature profiles over an urban airshed, *J. Geophys. Res.*, *103*, 10,593–10,604.
Jacobson, M. Z. (2001), Global direct radiative forcing due to multicomponent anthropogenic and natural aerosols, *J. Geophys. Res.*, *106*, 1551–1568.
Kallos, G., V. Kotroni, K. Lagouvardos, and A. Papadopoulos (1998), On the long-range transport of air pollutants from Europe to Africa, *Geophys. Res. Lett.*, *25*(5), 619–622.
Klein, H., et al. (2010), Saharan dust and ice nuclei over Central Europe, *Atmos. Chem. Phys.*, *10*, 10,211–10,221, doi:10.5194/acp-10-10211-2010.
Klemp, J. B., and R. B. Wilhelmson (1978), The simulation of three-dimensional convective storm dynamics, *J. Atmos. Sci.*, *35*, 1070–1096.
Lau, K. M., and M. Kim (2007), How Nature foiled the 2006 hurricane forecasts, *Eos Trans. AGU*, *88*, 105–107.
Leeuw, G., F. P. Neele, M. Hill, M. H. Smith, and E. Vignali (2000), Production of sea spray aerosol in the surf zone, *J. Geophys. Res.*, *105*, 29,397–29,409.
Lelieveld, J., et al. (2002), Global air pollution crossroads over the Mediterranean, *Science*, *298*, 794–799.
Levin, Z., A. Teller, E. Ganor, and Y. Yin (2005), On the interactions of mineral dust, sea salt particles and clouds – A measurement and modeling study from the MEIDEX campaign, *J. Geophys. Res.*, *110*, D20202, doi:10.1029/2005JD005810.

Li, G., Zhang, R., and Fan, J. (2005), Impacts of black carbon aerosol on photolysis and ozone, *J. Geophys. Res.*, *110*, D23206, doi:10.1029/2005JD005898.
Li, J., X. Ma, K. von Slazen, and S. Dobbie (2008), Parameterization of sea-salt optical properties and physics of the associated radiative forcing, *Atmos. Chem. Phys.*, *8*, 4787–4798.
Li, G., M. Zavala, W. Lei, A. P. Tsimpidi, V. A. Karydis, S. N. Pandis, M. R. Canagaratna, and L. T. Molina (2011), Simulations of organic aerosol concentrations in Mexico City using the WRF-CHEM model during the MCMA-2006/MILAGRO campaign, *Atmos. Chem. Phys.*, *11*, 3789–3809, doi:10.5194/acp-11-3789-2011.
Liao, H., and J. H. Seinfeld (1998), Radiative forcing by mineral dust aerosols: sensitivity to key variables, *J. Geophys. Res.*, *103*, 31,637–31,645.
Liao, H., Y. L. Yung, and J. H. Seinfeld (1999), Effects of aerosols on tropospheric photolysis rates in clear and cloudy atmospheres, *J. Geophys. Res.*, *104*, 23,697–23,707.
Lohmann, U., and J. Feichter (2005), Global indirect aerosol effects: A review, *Atmos. Chem. Phys.*, *5*, 715–737.
Lundgren, K., B. Vogel, H. Vogel, and C. Kottmeier (2013), Direct radiative effects of sea salt for the Mediterranean Region at conditions of low to moderate wind speeds, *J. Geophys. Res. Atmos.*, *118*, 1906–1923, doi:10.1029/2012JD018629.
Madronich, S. (1987), Photodissociation in the atmosphere: 1. Actinic flux and the effects of ground reflections and clouds, *J. Geophys. Res.*, *92*, 9740–9752.
Mallet, M., P. Tulet, D. Serça, F. Solmon, O. Dubovik, J. Pelon, V. Pont, and O. Thouron (2009), Impact of dust aerosols on the radiative budget, surface heat fluxes, heating rate profiles and convective activity over West Africa during March 2006, *Atmos. Chem. Phys.*, *9*, 7143–7160, doi:10.5194/acp-9-7143-2009.
Martin, R. V., D. J. Jacob, R. M. Yantosca, and M. Chin (2003), Global and regional decreases in tropospheric oxidants from photochemical effects of aerosols, *J. Geophys. Res.*, *108*(D3), 4097, doi:10.1029/2002JD002622.
McFarlane, S. A., E. I. Kassianov, J. Barnard, C. Flynn, and T. P. Ackerman (2009), Surface shortwave aerosol radiative forcing during the Atmospheric Radiation Measurement Mobile Facility deployment in Niamey, Niger, *J. Geophys. Res.*, *114*, D00E06, doi:10.1029/2008JD010491.
Mellor, G. L., and T. Yamada (1982), Development of a turbulence closure model for geophysical fluid problems, *Rev. Geophys.*, *20*(4), 851–875, doi:10.1029/RG020i004p00851.
Meyers, M. P., R. L. Walko, J. Y. Harrington, and W. R. Cotton (1997), New RAMS cloud microphysics parameterization, Part II: The two-moment scheme, *Atmos. Res.*, *45*, 3–39.
Mitsakou, C., G. Kallos, N. Papantoniou, C. Spyrou, S. Solomos, M. Astitha, and C. Housiadas (2008), Saharan dust levels in Greece and received inhalation doses, *Atmos. Chem. Phys. Disc.*, *8*, 7181–7192.
Mlawer, E. J., S. J. Taubman, P. D. Brown, M. J. Iacono, and S. A. Clough (1997), RRTM, a validated correlated-k model for the longwave, *J. Geophys. Res.*, *102*, 16,663–16,682.
Mohalfi, S., H. S. Bedi, T. N. Krishnamurti, and S. D. Cocke (1998), Impact of shortwave radiative effects of dust aerosols on the summer season heat low over Saudi Arabia, *Mon. Weather Rev.*, *126*, 3153–3168.
Monahan, E. C., D. E. Spiel, and K. L. Davidson (1986), A model of marine aerosol generation via whitecaps and wave disruption, in *Oceanic Whitecaps and Their Role in Air-Sea Exchange Processes*, edited by E. C. Monahan, G. MacNiocaill, and D. Reidel, pp. 167–174, Norwell, Mass.
Murazaki, K., and P. Hess (2006), How does climate change contribute to surface ozone change over the United States?, *J. Geophys. Res.*, *111*(D5), D05301, doi:10.1029/2005JD005873.
Nenes, A., and J. H. Seinfeld (2003), Parameterization of cloud droplet formation in global climate models, *J. Geophys. Res.*, *108*(D14), 4415, doi:10.1029/2002JD002911.
Nenes, A., C. Pilinis, and S. N. Pandis (1998), ISORROPIA: A new thermodynamic model for multiphase multicomponent inorganic aerosols, *Aquat. Geochem.*, *4*, 123–152.
Nenes, A., R. J. Charlson, M. C. Facchini, M. Kulmala, A. Laaksonen, and J. H. Seinfeld (2002), Can chemical effects on cloud droplet number rival the first indirect effect?, *Geophys. Res. Lett.*, *29*(17), 1848, doi:10.1029/2002GL015295.
Olivier, J., A. Bouwman, J. Berdowski, J. Bloos, A. Visschedijk, C. van der Mass, and P. Zandveld (1999), Sectoral emission inventories of greenhouse gases for 1990 on a per country basis as well as on 1 x 1 degrees, *Environ. Sci. Policy*, *2*, 241–263.
Perez C., S. Nickovic, J. M. Baldasano, M. Sicard, F. Rocadenbosch, and V. E. Cachorro (2006), A long Saharan dust event over the western Mediterranean: Lidar, Sun photometer observations, and regional dust modelling, *J. Geophys. Res.*, *111*, D15214, doi:10.1029/2005JD006579.
Quijano, A. L., I. N. Sokolik, and O. B. Toon (2000), Radiative heating rates and direct radiative forcing by mineral dust in cloudy atmospheric conditions, *J. Geophys. Res.*, *105*(D10), 12,207–12,219.
Quinn, P. K., and T. S. Bates (2005), Regional aerosol properties: Comparisons of boundary layer measurements from ACE 1, ACE 2, Aerosols99, INDOEX, ACE Asia, TARFOX, and NEAQS, *J. Geophys. Res.*, *110*, D14202, doi:10.1024/2004JD004755.
Real, E., and K. Sartelet (2011), Modeling of photolysis rates over Europe: Impact on chemical gaseous species and aerosols, *Atmos. Chem. Phys.*, *11*, 1711–1727, doi:10.5194/acp-11-1711-2011.
Rosenfeld, D., U. Lohmann, G. B. Raga, C. D. O'Dowd, M. Kulmala, S. Fuzzi, A. Reissell, and M. O. Andreae (2008), Flood or drought: How do aerosols affect precipitation?, *Science*, *321*, 1309, doi:10.1126/science.1160606.
Schell, B., I. J. Ackermann, H. Hass, F. S. Binkowski, and A. Ebel (2001), Modeling the formation of secondary organic aerosol within a comprehensive air quality model system, *J. Geophys. Res.*, *106*, 28,275–28,293.
Solomos, S., G. Kallos, J. Kushta, M. Astitha, C. Tremback, A. Nenes, and Z. Levin (2011), An integrated modeling study on the effects of mineral dust and sea salt particles on clouds and precipitation, *Atmos. Chem. Phys.*, *11*, 873–892, doi:10.5194/acp11-873-2011.
Solomos, S., G. Kallos, E. Mavromatidis, and J. Kushta (2012), Density currents as a desert dust mobilization mechanism, *Atmos. Chem. Phys.*, *12*, 11,199–11,211.
Spyrou, C., Mitsakou, C., Kallos, G., Louka, P. and Vlastou, G. (2010), An improved limited area model for describing the dust cycle in the atmosphere, *J. Geophys. Res.*, *115*, D17211, doi:10.1029/2009JD013682.
Spyrou, C., G. Kallos, C. Mitsakou, P. Athanasiadis, C. Kalogeri, and M. J. Iacono (2013), Modeling the radiative effects of desert dust on weather and regional climate, ACP. www.atmos-chem-phys.net/13/5489/2013, doi:10.5194/acp-13-5489-2013.
Stanelle, T., B. Vogel, H. Vogel, D. Bäumer, and C. Kottmeier (2010), Feedback between dust particles and atmospheric processes over West Africa during dust episodes in March 2006 and June 2007, *Atmos. Chem. Phys.*, *10*, 10,771–10,788, doi:10.5194/acp-10-10771-2010.
Stockwell, W. R., and W. S. Goliff (2004), Measurement of actinic flux and the calculation of photolysis rate parameters for the Central California Ozone Study, *Atmos. Environ.*, *38*, 5169–5177.
Tang, Y., et al. (2003), Impacts of aerosols and clouds on photolysis frequencies and photochemistry during TRACE-P, Part II: Three-dimensional study using a regional chemical transport model, *J. Geophys. Res.*, *108*(D21), 8822, doi:10.1029/2002JD003100.

Tegen, I., and A. A. Lacis (1996), Modeling of particle size distribution and its influence on the radiative properties of mineral dust aerosol, *J. Geophys. Res.*, *101*, 19,237–19,244.

Teller, A., and Z. Levin (2006), The effects of aerosols on precipitation and dimensions of subtropical clouds; a sensitivity study using a numerical cloud model, *Atmos. Chem. Phys.*, *6*, 67–80.

Teller, A., L. Xue, and Z. Levin (2012), The effects of mineral dust particles, aerosol regeneration and ice nucleation parameterizations on clouds and precipitation, *Atmos. Chem. Phys.*, *12*, 9303–9320.

van Aardenne, J., F. Dentener, J. Olivier, C. K. Goldewijk, and J. Lelieveld (2001), A 1 × 1 resolution data set of historical anthropogenic trace gas emissions for the period 1890- 1990, *Global Biogeochem. Cycles*, *15*(4), 909–928.

van den Heever, S. C., G. G. Carrio, W. R. Cotton, P. J. DeMott, and A. J. Prenni (2006), Impacts of nucleating aerosol on Florida storms. Part I: Mesoscale simulations, *J. Atmos. Sci.*, *63*, 1752–1775.

van den Heever, S. C., and W. R. Cotton (2007), Urban aerosol impacts on downwind convective storms, *J. Appl. Meteor. Climatol.*, *46*, 828–850.

Vogel B., H. Vogel, D. Bäumer, M. Bangert, K. Lundgren, R. Rinke, and T. Stanelle (2009), The comprehensive model system COSMO-ART: Radiative impact of aerosol on the state of the atmosphere on the regional scale, *Atmos. Chem. Phys.*, *9*, 8661−8680.

Walcek, C. J., and G. R. Taylor (1986), A theoretical method for computing vertical distributions of acidity and sulfate production within cumulus clouds, *J. Atmos. Sci.*, *43*, 439–455.

Walko, R. L., W. R. Cotton, M. P. Meyers, and J. Y. Harrington (1995), New RAMS cloud microphysics parameterization. Part I: The single moment scheme, *Atmos. Res.*, *38*, 29–62.

Walko, R. L., et al. (2000), Coupled atmosphere-biophysics – hydrology models for environmental modelling, *J. Appl. Meteorol.*, *39*, 931–944.

Wesely, M. L. (1989), Parameterization of surface resistance to gaseous dry deposition in regional-scale numerical models, *Atmos. Environ.*, *23*, 1293–1304.

Zhang, K. M., E. M. Knipping, A. S. Wexler, P. V. Bhave, and G. S. Tonnesen (2005), Size distribution of sea-salt emissions as a function of relative humidity, *Atmos. Environ.*, *39*, 3373–3379.